Scientific Data

https://doi.org/10.1038/s41597-026-08095-1

Article in Press

A longitudinal data resource to study brain development and transdiagnostic variation in executive function

Received: 14 May 2026

Accepted: 10 August 2026

Published online: 20 August 2026

Cite this article as: Sevchik, B.L., Shafiei, G., Murtha, K. *et al.* A longitudinal data resource to study brain development and transdiagnostic variation in executive function. *Sci Data* (2026). https://doi.org/10.1038/s41597-026-08095-1

Brooke L. Sevchik, Golia Shafiei, Kristin Murtha, Sophia Linguiti, Lia Brodrick, Juliette B. H. Brook, Matt Cieslak, Elizabeth Flook, Kahini Mehta, Steven L. Meisler, Kosha Ruparel, Sage Rush, Taylor Salo, S. Parker Singleton, Tien T. Tong, Mrugank Salunke, Dani S. Bassett, Monica E. Calkins, Mark A. Elliott, Raquel E. Gur, Ruben C. Gur, Tyler M. Moore, J. Cobb Scott, Russell T. Shinohara, M. Dylan Tisdall, Daniel H. Wolf, David R. Roalf & Theodore D. Satterthwaite

We are providing an unedited version of this manuscript to give early access to its findings. Before final publication, the manuscript will undergo further editing. Please note there may be errors present which affect the content, and all legal disclaimers apply.

If this paper is publishing under a Transparent Peer Review model then Peer Review reports will publish with the final article.

ARTICLE IN PRESS

© The Author(s) 2026. **Open Access** This article is licensed under a Creative Commons Attribution 4.0 International License, which permits use, sharing, adaptation, distribution and reproduction in any medium or format, as long as you give appropriate credit to the original author(s) and the source, provide a link to the Creative Commons licence, and indicate if changes were made. The images or other third party material in this article are included in the article's Creative Commons licence, unless indicated otherwise in a credit line to the material. If material is not included in the article's Creative Commons licence and your intended use is not permitted by statutory regulation or exceeds the permitted use, you will need to obtain permission directly from the copyright holder. To view a copy of this licence, visit http://creativecommons.org/licenses/by/4.0/.

ARTICLE IN PRESS

A longitudinal data resource to study brain development and transdiagnostic variation in executive function

Brooke L. Sevchik[1,2,3], Golia Shafiei[1,2,3], Kristin Murtha[1,2,3,4], Sophia Linguiti[1,2], Lia Brodrick[1,2,3,5], Juliette B.H. Brook[1,2,3], Matt Cieslak[1,2,3], Elizabeth Flook[2,6], Kahini Mehta[1,2,3,7], Steven L. Meisler[1,2,3], Kosha Ruparel[2], Sage Rush[1,2,3], Taylor Salo[1,2,3], S. Parker Singleton[1,2,3], Tien T. Tong[1,2,3], Mrugank Salunke[2], Dani S. Bassett[2,8,9,10,11,12], Monica E. Calkins[2,3], Mark A. Elliott[13], Raquel E. Gur[2,3,6,8,13], Ruben C. Gur[2,3,8,13], Tyler M. Moore[2,3], J. Cobb Scott[2,14], Russell T. Shinohara[15,16], M. Dylan Tisdall[13], Daniel H. Wolf[2,3,16], David R. Roalf[2,3], Theodore D. Satterthwaite[1,2,3 *]

[1]Penn Lifespan Informatics and Neuroimaging Center, University of Pennsylvania, PA, USA

[2]Department of Psychiatry, Perelman School of Medicine, University of Pennsylvania, PA, USA

[3]Penn-CHOP Lifespan Brain Institute, Perelman School of Medicine, Children's Hospital of Philadelphia Research Institute, Philadelphia, PA, USA

[4]Department of Psychology, University of Pennsylvania, Philadelphia, PA, USA

[5]New York University, New York, NY, USA

[6]Department of Child and Adolescent Psychiatry and Behavioral Science, Children's Hospital of Philadelphia, Philadelphia, PA, USA

[7]Department of Neuroscience, Columbia University, New York, NY, USA

[8]Department of Neurology, University of Pennsylvania, Philadelphia, PA, USA

[9]Department of Bioengineering, University of Pennsylvania, Philadelphia, PA, USA

[10]Department of Electrical and Systems Engineering, University of Pennsylvania, Philadelphia, PA, USA

[11]Department of Physics and Astronomy, University of Pennsylvania, Philadelphia, PA, USA

[12]Santa Fe Institute, Santa Fe, NM, USA

[13]Department of Radiology, University of Pennsylvania, Philadelphia, PA, USA

[14]VISN4 Mental Illness Research, Education, and Clinical Center at the Crescenz VA Medical Center, Philadelphia, PA, USA

[15]Penn Statistics in Imaging and Visualization Center, Department of Biostatistics, Epidemiology, and Informatics, University of Pennsylvania, Philadelphia, PA, USA

[16]Center for Biomedical Image Computing and Analytics, University of Pennsylvania, Philadelphia, PA, USA

*Corresponding author: Theodore D. Satterthwaite
Email address: sattertt@pennmedicine.upenn.edu
Address: 3700 Hamilton Walk, 5A, Philadelphia, PA 19104

ARTICLE IN PRESS

Abstract

Executive function (EF) develops rapidly during adolescence. However, deficits in EF also emerge in adolescence, representing a transdiagnostic symptom associated with many forms of psychopathology. To promote transdiagnostic research on EF during development, we introduce a new data resource – the Penn Longitudinal Executive functioning in Adolescent Development study (Penn LEAD) – that combines longitudinal multimodal imaging data with rich clinical and cognitive phenotyping. These data include 225 imaging sessions from 132 individuals (8-16 years old at the time of enrollment) who are typically developing (27.3%), or meet criteria for attention-deficit hyperactivity disorder (20.5%) or the psychosis-spectrum (52.3%). In addition to phenotypic data from multiple cognitive tasks focused on EF, the study includes data from structural MRI, diffusion MRI, *n*-back task fMRI, resting-state fMRI, and arterial spin-labeled MRI. Notably, all raw data, fully-processed derived data, and detailed quality control recommendations are publicly shared on OpenNeuro. We anticipate that such analysis-ready data will accelerate research on EF development in psychiatry.

Key Words:

- Executive function
- Cognition
- ADHD
- Psychosis
- Neuroimaging
- Adolescence
- Development
- Longitudinal
- MRI
- Open access

ARTICLE IN PRESS

ARTICLE IN PRESS

Background & Summary

Executive function (EF) is a broad cognitive domain, encompassing multiple component processes such as attentional control, working memory, abstraction, and set shifting. EF undergoes protracted development during adolescence and young adulthood as higher-order association cortex matures. [1–3] Deficits in EF often emerge in adolescence and are a major transdiagnostic domain of impairment across many forms of psychopathology. [4–7] EF deficits notably play a central role in attention-deficit hyperactivity disorder (ADHD) and psychosis-spectrum (PS) disorders.[8–10] In these disorders and others, lower EF has been linked to greater rates of interpersonal conflict and poorer academic outcomes. [11–16] In this context, we introduce a new, open-access longitudinal data resource – Penn LEAD (Penn Longitudinal Executive functioning in Adolescent Development) – focused on EF in PS and ADHD.

This data resource is motivated by two gaps in the literature. First, while previous neuroimaging research in adults[17] and children[18] has emphasized EF as a key marker of psychopathology, there are relatively few longitudinal neuroimaging data resources in adolescents with psychiatric disorders enriched for executive dysfunction. This lack of longitudinal open data is notable, given the short-comings of cross-sectional data in capturing the dynamic trajectories of developmental processes and the onset of mental health disorders that often occurs in adolescence.[19] The need for longitudinal data is especially pertinent to studies of executive function, given its protracted development throughout childhood, adolescence, and young adulthood.[20] Many of the existing longitudinal datasets in adolescents focus mainly on healthy participants, excluding those with psychiatric disorders (developing Chinese Color Nest Project[21]; Lifespan Human Connectome Project Development[22]; NIH-MRI of Normal Brain Development[23]). The datasets that are focused on adolescent participants with psychiatric diagnoses often lack a wide breadth of multimodal imaging data, such as multi-shell diffusion-weighted imaging (DWI) and arterial spin-labeled MRI (ASL) (1000 Functional Connectomes Project[24]; ADHD-200 Consortium[25]; Healthy Brain Network[26]; North American Prodrome Longitudinal Study[27]; Oregon ADHD-1000[28]; Reproducible Brain Charts[29]). Although the Adolescent Brain Cognitive Development Study[30,31], NKI-Rockland,[32,33] and IMAGEN[34] datasets provide rich multimodal data, they have relatively coarse measures of EF and were not specifically designed to assess EF development in the context of psychopathology.

A second gap that this resource seeks to address is the need for datasets that contain easily accessible, quality-controlled, analysis-ready data. Most datasets are restricted by cumbersome data-use agreements (DUAs) that can impede rapid progress.[29,35–41] Furthermore, many multimodal longitudinal imaging studies focused on adolescents with psychiatric disorders provide only raw or minimally-preprocessed data.[30,31,34] The lack of easily-accessible, fully-processed derivatives increases computational burden on researchers, leads to redundant efforts across research groups, and makes it difficult to reconcile disparate findings across studies.

To address these gaps, Penn LEAD combines longitudinal, fully-processed, multimodal imaging data with extensive cognitive and clinical phenotyping focused on EF. Multimodal neuroimaging data includes structural magnetic resonance imaging (sMRI), diffusion-weighted

ARTICLE IN PRESS

imaging (DWI), functional MRI (fMRI; resting-state and *n*-back task), ASL, and a multi-echo gradient-recalled echo sequence (MEGRE) for quantitative susceptibility mapping (QSM). In addition to raw data, this data resource includes fully-processed, derived data from open-source workflows as well as detailed assessments of image quality. To maximize reproducibility, all processed data were generated using the "FAIRly-big" framework,[42] which provides full provenance-tracking with DataLad.[43] Anonymized data are openly available on OpenNeuro[44] without a DUA, which removes barriers to data access and facilitates replication of analyses between different research groups. As described below, we anticipate that this dataset will accelerate research on transdiagnostic variation of EF in adolescence.

Methods

Recruitment, Participants, and Procedures

Participants were identified and enrolled in the study across two study visits (see **Figure 1** for study timeline). First, participants were recruited from the Children's Hospital of Philadelphia (CHOP) patient population, via medical record review and referrals from outpatient behavioral health or primary care clinics. Our target population included youth between 8-16 years old. Exclusion criteria consisted of: 1) metallic implants, claustrophobia, or other contraindications to MRI; 2) significant medical or neurological illness that impacted brain function or impeded participation; 3) acute intoxication with alcohol or other substances based on clinical assessment or participant report; and 4) pregnancy. Participant demographics are detailed in **Figure 2c**. Participants were invited to participate in a two-stage research study involving neuroimaging as well as clinical and cognitive phenotyping. Participants were recruited from three groups: attention-deficit hyperactivity disorder (ADHD group), clinical high risk for psychosis (PS group), and typically developing adolescents without any clinical diagnosis (TD group). Any participant with co-morbid ADHD and PS were included with the PS group. These recruitment groups were confirmed via thorough clinical diagnostic procedures detailed below.

Subsequently, youth and their parents completed an initial 3-5 hour clinical visit during which participants received a detailed diagnostic assessment from trained assessors[45] (**Figure 2b; Table 1)**. Parents provided collateral information for all participants; children over the age of eleven years were also interviewed about their own symptoms. The computerized assessment combined a modified and adapted version of Kiddie Schedule for Affective Disorders and Schizophrenia (K-SADS[46]; see Calkins et al., 2017[47] for details on the modifications) as well as the Structured Interview for Prodromal Symptoms (SIPS[48]). These clinical procedures provided details of all co-morbid diagnoses in addition to the diagnoses indicated by recruitment groups. Note that for co-morbid diagnoses, psychosis spectrum disorders were broken down into subthreshold psychosis (those with clinical high risk for psychosis), and full threshold psychosis. During this first visit, participants also completed a broad battery of cognitive tasks[49–54] (see

Cognitive Assessment, below). Diagnostic and neurocognitive testing information was collected from *N* = 132 participants (49.2% female; average age at intake = 11.9 years).

On the second visit, youth were invited to participate in neuroimaging procedures if the semi-structured diagnostic assessment during the first visit indicated that they met criteria for one of three diagnostic groups. Specifically, youth were asked to participate in neuroimaging if they met criteria for ADHD, PS, or were typically-developing (TD, i.e., no current or lifetime history of any DSM-V diagnosis). Co-morbidity was permitted; participants meeting criteria for both PS and ADHD diagnoses were considered in the psychosis-spectrum study group for enrollment purposes.

Participants completed a 4-5 hour neurocognitive and neuroimaging visit at each longitudinal timepoint, with one to three neuroimaging visits per participant (average time between sessions = 648.5 days; **Figure 2a**). At each neuroimaging visit participants completed cognitive testing focused on executive functioning tasks (see **Cognitive Assessment**) and a battery of self-report surveys (see **Self-Report Data**). Participants with a second and/or third neuroimaging visit repeated the same battery of cognitive tests as during their first visit. In total, this dataset includes 225 neuroimaging sessions from *N* = 132 participants (49.2% female, average age across all scans = 13.4 years).

Ethics Statement

During the first visit, informed consent for study procedures was provided by the parent or guardian of minor participants; minor participants provided assent. The informed consent document contained language from the Open Brain Consent[55] to facilitate open data sharing. Study procedures were approved by the University of Pennsylvania and Children's Hospital of Philadelphia Institutional Review Boards (application number 829744).

Cognitive Assessment

Cognition was assessed with the Penn Computerized Neurocognitive Battery (Penn CNB.[49–53] In this study, we included both tasks measuring general cognition (Lifespan Brain Institute CNB; LiBI CNB) and a specialized suite of tasks focused on executive function ability (EF CNB). In total, these two batteries comprised 21 distinct tasks (**Table 2)**. For timepoint 1, the LiBI CNB was administered on the day of the clinical interview, and the EF CNB was administered on the day of the MRI scan. For longitudinal timepoints 2 and 3, both the LiBI CNB and the EF CNB were administered on the day of the MRI scan.

The CNB includes summary measures of cognitive performance based on accuracy and response time. These include a rich variety of measures, such as the median response times as well as the sum (and/or average) of correct responses, incorrect responses, true positives, false positives, false negatives, and true negatives. The data provided are not normalized. Detailed descriptions of each task can be found in the citations in **Table 2**.

Self-Report Data

All participants completed a broad array of self-report batteries (**Table 3**). Scales were grouped into main, pre-scan, and post-scan batteries. The main battery consisted of the Adverse Life Experiences Scale (ALES[56]), Affective Lability Scale (ALS-18[57]), Affective Reactivity Index (ARI[58]), Altman Self-Rating Mania Scale (ASRM[59]), Beck Depression Inventory (BDI-1A[60], modified child version without suicide item), Behavioral Inhibition/Activation System (BIS-BAS child version[61,62]), the Extended Strengths and Weaknesses Assessment of Attention-Deficit/Hyperactivity-Disorder Symptoms and Normal Behavior (E-SWAN ADHD[63,64]), the Extended Strengths and Weaknesses Assessment of Disruptive Mood Dysregulation Disorder Symptoms and Normal Behavior (E-SWAN DMDD[63]), The Motivation and Pleasure Scale - Self Report (MAP-SR[65]), Positive and Negative Affect Schedule (PANAS child[66]), PROMIS Pediatric Anxiety scale (PPA[67]), PRIME Screen (self-report),[68,69] Revised Physical Anhedonia Scale (RPAS[70]), Revised Social Anhedonia Scale (RSAS[70]), Substance Use Questionnaire,[71] Tanner Developmental Scale (Boy),[72] Tanner Developmental Scale (Girl),[73] and Wolf Intrinsic Motivation/Extrinsic Motivation Scale (Wolf IM/EM short version[74]). Descriptions of each scale can be found in the citations in **Table 3**. Participants completed the pre-scan battery before their MRI scan, consisting of the full State-Trait Anxiety Inventory (STAI[75]), and the post-scan battery after their MRI scan, consisting of only the state items (items 1-20) of the STAI after their MRI scan.

We release the raw self-report data with their summary scores (where applicable) for each session. We did not include summary scores for the Tanner Developmental Stages scales due to complexities in how puberty is staged, and we did not include summary scores for the Substance Use Questionnaire given the lack of participants who endorsed drug use and the complexity of substance use. Summary scores were calculated in accordance with guidelines from each scale's original publication, primarily by calculating the sums and averages of individual item-level data. For each scale, we did not calculate a summary score for a given session if it was missing any individual item. Scoring details are described in the JSON files accompanying each scale. The code used for scoring is also available publicly on GitHub (https://github.com/PennLINC/transdiagnostic_executive_function/tree/main/self_report).

Neuroimaging Data Acquisition

MRI data were acquired on a 3T Siemens Prisma scanner (Erlangen, Germany) with a 32-channel head coil at the University of Pennsylvania. The imaging protocol was approximately 60 minutes long. The full MRI protocol is provided as a PDF file on OpenNeuro, alongside the complete dataset. Prior to scanning, participants completed a brief practice version of the *n*-back task to prepare them for performing the same task in the MRI scanner.

During the scan, participants were placed supine in the scanner and were given earplugs and head padding to both muffle noise and reduce head motion. Sequences included sMRI T1-weighted (T1w) and T2-weighted (T2w) scans; fMRI resting-state and *n*-back task-based scans; ASL scans; DWI scans; and a MEGRE sequence for QSM (**Figure 3**). Raw imaging data includes a total of 223 T1w scans, 224 T2w scans, 213 resting-state fMRI scans, 209 task fMRI

scans, 188 ASL scans, 219 diffusion scans, and 181 MEGRE scans. A summary of sequence parameters is provided in **Table 4**.

Structural MRI

We first acquired T1w structural images using acquisition parameters that were highly similar to the ABCD study[30,31] (176 slices; repetition time, TR = 2500 ms; TI = 1070 ms; echo time, TE = 2.9 ms; flip angle, FA = 8°; field of view, FOV = 256 x 256 mm; matrix size = 256 x 256; voxel size = 1.0 mm; phase encoding direction = A >> P; acquisition time 7:12 min). Similarly, the T2w structural scan was harmonized with the ABCD study (176 slices; repetition time, TR = 3200 ms; echo time, TE = 565 ms; flip angle, FA = 120°; field of view, FOV = 256 x 256 mm; matrix size = 256 x 256; voxel size = 1.0 mm; phase encoding direction = A >> P; acquisition time 6:35 min). During structural scans, participants watched movie clips from *Harry Potter* or *Ratatouille*, depending on their preference.

Diffusion MRI

We also acquired a multi-shell, single spin-echo DWI sequence in the Posterior-to-Anterior phase encoding direction, using a monopolar sampling scheme, with acquisition parameters highly similar to the ABCD study[30,31] (repetition time, TR = 4200 ms; echo time, TE = 89 ms; field of view, FOV = 240 x 240 mm; matrix = 140 x 140; voxel size = isotropic 1.7 mm; 81 interleaved slices acquired posterior to anterior; a multiband factor of 3; acquisition time = 7:29 min). We acquired the following volumes: 7 at b = 0, 6 at b =500, 15 at b =1000, 15 at b =2000, and 60 at b = 3000 s/mm^2 (103 volumes total). These diffusion sequences were accompanied by an additional b = 0 scan acquired in both the Posterior-to-Anterior and Anterior-to-Posterior phase encoding directions (repetition time, TR = 12400 ms; echo time, TE = 89 ms; flip angle, FA = 90°; field of view, FOV = 240 x 240 mm; voxel size = isotropic 1.7 mm; 81 interleaved slices; multiband factor = 1; acquisition time = 0:25 min each) that were used to estimate a field map.

Functional MRI

Acquisition parameters for fMRI scans were also highly similar to the ABCD study.[30,31] We acquired one run of *n*-back task fMRI, two runs of resting-state fMRI, and accompanying field maps. During the fMRI *n*-back task run (single-echo; 60 slices; repetition time, TR = 800 ms; echo time, TE = 30 ms; flip angle, FA = 52°; field of view, FOV = 216 x 216 mm; matrix size = 90 x 90; voxel size = isotropic 2.4 mm; multiband factor = 6; in-plane acceleration factor = 1; 522 volumes; acquisition time = 7:02 min), participants completed a version of the *n*-back task with fractal images.[76,77] In the scanner, participants were shown a continuous sequence of fractal images and were instructed to press a button if the current image matched the image they saw *n* stimuli before. We used a modified version of the *n*-back task, during which participants completed the task for two working memory levels: 0-back, for which they pressed the button when the fractal image matched a specified target fractal image; and 2-back, for which they pressed the button if the fractal image matched the image from two trials before it. We did not

include an intermediate 1-back task. Scored task event files can be found with the raw fMRI data on OpenNeuro.

We also acquired two runs of fMRI where participants were asked to view a fixation cross (60 slices; repetition time, TR = 800 ms; echo time, TE = 30 ms; FA=52°; FOV = 216 mm; matrix size = 90 x 90; voxel size = isotropic 2.4 mm; multiband factor = 6; in-plane acceleration factor = 1). The first run (522 volumes, acquisition time = 7:02 min) was acquired before the fractal *n*-back task run; the second run (383 volumes, acquisition time = 5:11 min) was acquired after the fractal *n*-back task. In addition, field maps with one volume in both the Anterior-to-Posterior and Posterior-to-Anterior phase encoding direction were collected for distortion correction (60 slices; repetition time, TR = 7030 ms; echo time, TE = 80 ms; flip angle, FA = 90°; field of view, FOV = 216 x 216 mm; matrix size = 90 x 90; voxel size = isotropic 2.4 mm; acquisition time 0:14 min each).

Arterial spin-labeled MRI

We measured cerebral perfusion using an unbalanced, background-suppressed, 3D stack of spirals pseudo-continuous arterial spin-labeled (PCASL) MRI scan (labeling duration = 1500 ms; post-labeling delay, PLD = 1500 ms; repetition time, TR = 4298 ms; echo time, TE = 10 ms; field of view, FOV = 240 x 240 mm; voxel size = isotropic 3.8 mm; 80 volumes; acquisition time = 5:43 min). This acquisition was accompanied by a separate M0 reference scan with the same spatial parameters (repetition time, TR = 4000 ms; echo time, TE = 10.03 ms).

MEGRE

We also acquired a MEGRE sequence with four echoes (96 slices; repetition time, TR = 35 ms; echo times, TEs = 7.50, 15.00, 22.50, 30.00 ms; flip angle, FA = 15°; field of view, FOV = 240 x 180 mm; matrix size = 160 x 120; voxel size = isotropic 1.5 mm; phase encoding direction = R >> L; acquisition time 3:59 min). This scan can be used for QSM.

Neuroimaging Curation

We used CuBIDS software (Curation of BIDS[78]) to curate the raw neuroimaging data and metadata. CuBIDS allows for fully reproducible curation of metadata and file names in the BIDS dataset using DataLad.[43] Notably, BIDS Apps used for image processing are automatically configured based on the metadata they encounter. As such, if metadata are incorrect, preprocessing pipelines run the risk of being "reproducible but wrong." Accordingly, careful metadata curation with CuBIDS helps ensure accurate preprocessing pipelines, thereby reducing the potential for inaccurate preprocessing pipelines due to absent or incorrect metadata. All code for metadata curation is available on GitHub.

CuBIDS also helps identify sources of variation and heterogeneity in the imaging data. For each scan type, the 'Dominant Group' represents the subset of acquisition parameters that match the majority of files, whereas 'Variant Groups' denote the subset of scans with different acquisition parameters (**Table S1)**. For example, among *n*-back scans, *N* = 1 had a lower number

ARTICLE IN PRESS

of volumes than expected, and was assigned to a Variant Group. In contrast, the majority (*N* = 185) were acquired with the expected number of volumes with no other metadata variation, and assigned to the Dominant Group. The full CuBIDS summary file is available on OpenNeuro (ds007116, `code/` subfolder, v50). ASL scans have a lower percentage of scans (60.11%) in the dominant group; this is due to minor variances in effective echo spacing, repetition time, and total readout time. Most scans not in the dominant group for fMRI runs (11.5% for *n*-back, 12.1% for the first resting state run, 15.6% for the second resting state run) are due to small amounts of variation in scan obliquity or the number of volumes acquired.

Image Processing

As data are openly shared, maintaining participant data privacy is of paramount concern. Accordingly, we anonymized structural images using AFNI's refacer[79] for the T1w images and Pydeface v2.0.2[80] for the T2w images. Following anonymization, we utilized BIDS Apps[81] for image processing including sMRIPrep,[82–84] fMRIPrep,[82–84] QSIPrep,[85] QSIRecon,[85] and ASLPrep.[86,87] All BIDS Apps for image processing were run via the BIDS-App Bootstrap software (BABS[88]) that uses DataLad[43] to provide a full audit trail and enhance reproducibility. We utilized the University of Pennsylvania's CUBIC computing resource, a RedHatEnterprise Linux-based HPC cluster. Note that we did not complete any processing of the MEGRE scans; the raw data is available on OpenNeuro. **Figure 4** describes the number of scans available at each stage, including raw data, processed images, and scans passing quality control (QC; see **Quality Control**). Detailed information on image processing compiled below are derived from methods descriptions generated by each BIDS App, under the CC0 1.0 Universal license.

Structural image processing

Anatomical images were processed using sMRIPrep, executed as the anatomical-only option in fMRIPrep v25.0.0[83,83,84] based on Nipype v1.9.2[89,90]. Using the sMRIPrep workflow allowed us to use the anatomical outputs in multiple downstream workflows, such as fMRIPrep and ASLPrep. As part of sMRIPrep, the T1w image was corrected for intensity non-uniformity (INU) with N4BiasFieldCorrection[91] with ANTs 2.5.4.[92] The image was then skull-stripped with a Nipype implementation of the antsBrainExtraction.sh workflow. Brain tissue segmentation was performed on the brain-extracted T1w using fast (FSL v6.0.7.7[93]). Brain surfaces were reconstructed using FreeSurfer's recon-all workflow (FreeSurfer 7.3.2[94]). The brain mask estimated previously with the ANTs brain extraction was refined to reconcile ANTs-derived and FreeSurfer-derived segmentations. The T2w image was used to improve pial surface refinement. Volume-based spatial normalization to two standard spaces (MNI152NLin6Asym, MNI152NLin2009cAsym) was performed using antsRegistration (ANTs 2.5.4), using brain-extracted versions of both T1w reference and the T1w template. Grayordinate "dscalar" files containing 91k grayordinates were resampled onto fsLR 32K space using Connectome

ARTICLE IN PRESS

Workbench.[95] Outputs from sMRIPrep were further processed using freesurfer-post v0.1.2 (https://github.com/PennLINC/freesurfer-post.git). Freesurfer-post parcellates and then aggregates morphometric measures from FreeSurfer into tabulated data to facilitate cross-modality comparisons. FreeSurfer data was parcellated using multiple common atlases as described below (see **Atlases**).

Functional image pre-processing

We preprocessed fMRI data using fMRIPrep v25.0.0,[82–84] which is based on Nipype v1.9.2.[89,90] For each blood-oxygen level dependent (BOLD) run per subject, across all tasks and sessions, the following preprocessing was performed. First, a reference volume was generated for use in head motion correction. Head-motion parameters with respect to the BOLD reference (transformation matrices and six corresponding rotation and translation parameters) are estimated before any spatiotemporal filtering using mcflirt (FSL v6.0.7.7[96]). The BOLD reference was then co-registered to the T1w reference using bbregister (FreeSurfer), with six degrees of freedom. The aligned T2w image was used for initial co-registration. The BOLD time series were resampled onto the left/right-symmetric template "fsLR" using Connectome Workbench.[97] Grayordinates files[97] containing 91k samples were also generated with surface data transformed directly to fsLR 32K space and subcortical data transformed to 2 mm resolution MNI152NLin6Asym space.

Functional image post-processing

Following preprocessing with fMRIPrep, fMRI data was post-processed using XCP-D v0.10.7,[98–100] which was built with Nipype v1.10.0.[89,90] Many internal operations of XCP-D use AFNI,[79,101] Connectome Workbench,[102] ANTS,[92] TemplateFlow v24.2.2,[103] matplotlib v3.10.0,[104] Nibabel v5.3.2,[105] Nilearn v0.11.1,[106] numpy v2.2.1,[107] pybids v0.18.1,[108] and scipy v1.15.1.[109]

For each fMRI run that was successfully processed with fMRIPrep, the following post-processing was performed using XCP-D. Non-steady-state volumes were extracted from the preprocessed confounds and were discarded from both the BOLD data and nuisance regressors. The BOLD data were converted to NIfTI format, despiked with AFNI's 3dDespike, and converted back to CIFTI format. Nuisance regressors were regressed from the BOLD data using a denoising method based on Nilearn's approach. The time series were band-pass filtered using a second-order Butterworth filter, in order to retain signals between 0.01-0.08 Hz; the same filter was applied to the confounds. The resulting time series were then denoised using linear regression. Task data was post-processed in the same manner as resting-state data without accounting for task-related activation in denoising. Processed functional time series were calculated for parcels in a wide range of atlases (see **Atlases** below) using Connectome Workbench. In cases of partial coverage, uncovered vertices (values of all zeros or NaNs) were

ARTICLE IN PRESS

either ignored (when the parcel had >50.0% coverage) or were set to zero (when the parcel had <50.0% coverage). Inter-regional functional connectivity between all regions was computed for each atlas as the Pearson correlation between unsmoothed time series of parcel pairs using Connectome Workbench. Denoised BOLD was then smoothed using Connectome Workbench[102] with a Gaussian kernel (full width at half maximum (FWHM) = 6 mm); as noted above, smoothing was applied after parcel time series were extracted for each atlas to avoid blurring across parcel borders.

Additionally, XCP-D outputs include the Amplitude of Low Frequency Fluctuations (ALFF[110]) and Regional Homogeneity (ReHo[111]). ALFF was computed by transforming the mean-centered, standard deviation-normalized, denoised BOLD time series to the frequency domain. The power spectrum was computed within the 0.01-0.08 Hz frequency band and the mean square root of the power spectrum was calculated at each voxel or vertex to estimate ALFF. The resulting ALFF values were then multiplied by the standard deviation of the denoised BOLD time series to retain the original scaling. ALFF maps were smoothed with the Connectome Workbench using a Gaussian kernel (FWHM = 6 mm). In addition, for each hemisphere, ReHo was computed using surface-based 2dReHo.[112] Specifically, for each vertex on the surface, Kendall's coefficient of concordance (KCC) was computed with nearest-neighbor vertices to yield ReHo. For the subcortical, volumetric data, ReHo was computed with neighborhood voxels using AFNI's 3dReHo.[113]

Task fMRI modeling

We used Nilearn[114] to fit first-level generalized linear models for fMRI data collected during the fractal *n*-back task (one run per participant). The model included regressors for both the 2-back and 0-back conditions. In the response time-duration model, we included a regressor that models trial onsets with durations equal to participants' response times (RTDur), following the ConsDurRTDur model described in Mumford et al.[115] We calculated participant-level effect size maps for the 2-back > 0-back, 2-back > baseline, and 0-back > baseline contrasts. We then used these maps to perform a group-level analysis in Nilearn. Statistical inferences were based on non-parametric permutation testing (10,000 permutations) with voxel family-wise error (FWE) correction (two-sided, $p < 0.05$, cluster-forming threshold $p < 0.001$).

We also compared the group-level 2-back > 0-back contrast results from our data with results from a similar fractal *n*-back task administered as part of the Philadelphia Neurodevelopmental Cohort (PNC[116]). Both second-level maps (visualized as z-statistics) were defined in the MNI152 space, then resampled to the fsLR surface and parcellated into 400 cortical regions using the Schaefer 400 atlas[117] with Neuromaps.[118,119] We quantified the spatial correlation with the PNC group-level task contrast map using a Pearson correlation. To test the spatial correspondence of these maps, we used the Alexander-Bloch rotation method (i.e., spin

ARTICLE IN PRESS

test[120]). Specifically, we compared the empirical spatial correlation between maps to a null distribution generated using 10,000 spatial autocorrelation-preserving null maps.

Diffusion image processing

We used QSIPrep v1.0.0[85] based on Nipype v1.9.1,[89,90] to preprocess DWI data. Many internal operations of QSIPrep use Nilearn v0.10.1[106] and Dipy.[121] First, the anatomical reference image was reoriented into AC-PC alignment (an orientation based on the anterior and posterior commissures) via a 6-DOF transform extracted from a full Affine registration to the MNI152NLin2009cAsym template. A full nonlinear registration to the template from AC-PC space was estimated via symmetric nonlinear registration (SyN) using antsRegistration. Brain extraction was performed on the T1w image using SynthStrip[122] and automated segmentation was performed using SynthSeg[123] from FreeSurfer v7.3.1.

DWI data were denoised using the Marchenko-Pastur PCA method implemented in dwidenoise[124–127] with an automatically-determined window size of 3 voxels. After MP-PCA, Gibbs ringing was removed using TORTOISE.[128,129] Any images with a *b*-value less than 100 s/mm^2 were treated as a $b = 0$ image. FSL's eddy was used for head motion correction and eddy current correction.[130] Eddy was configured with a *q*-space smoothing factor of 10, a total of 5 iterations, and 1000 voxels used to estimate hyperparameters. A quadratic first level model and a linear second level model were used to characterize Eddy current-related spatial distortion. Field offset was attempted to be separated from subject movement. *Q*-space coordinates were forcefully assigned to shells; shells were aligned post-eddy. Eddy's outlier replacement was run.[131]. As part of outlier replacement, data were grouped by slice, only including values from slices determined to contain at least 250 intracerebral voxels. Groups of voxels deviating by more than 4 standard deviations from the prediction had their data replaced with imputed values. Final interpolation was performed using the Jacobian modulation method.

Framewise displacement (FD) was calculated using the implementation in Nipype (following the definitions by Power et al., 2014[132]). The head-motion estimates calculated in the correction step were also placed within the corresponding confounds file. Slicewise cross correlation was also calculated. The DWI time series were resampled to AC-PC, generating a preprocessed DWI run in AC-PC space with 1.7 mm isotropic voxels. We also calculated Neighboring DWI Correlation (NDC[133]), a metric of DWI image quality[134] that measures the mean spatial correlation of a volume between its neighbors in *q*-space.

After preprocessing with QSIPrep, the preprocessed DWI images were reconstructed using multiple complementary methods using QSIRecon v1.1.0,[85] which is based on Nipype v1.9.1.[89,90] QSIRecon implements multiple models of diffusion data to calculate a rich variety of whole-brain parametric microstructure maps. Brain masks from SynthStrip were used in all subsequent reconstruction steps.

ARTICLE IN PRESS

First, matching the workflow from the ABCD study,[30,31,135] we computed a "full shell" tensor fit[136] using data from all *b*-values, using 'EstimateTensor' with WLLS regularization. This model is widely used to model Gaussian diffusion data and calculates scalar maps including fractional anisotropy (FA), mean diffusivity (MD), axial diffusivity (AD), and radial diffusivity (RD). These images can be found in the `qsirecon-TORTOISE_model-tensor` directory.

Second, we implemented diffusion kurtosis imaging (DKI[137,138]), which fits a fourth-order tensor such that it might be more accurate in cases of non-Gaussian diffusion. DKI fits a model using the full shell with all *b*-values, calculating scalar maps including FA, MD, AD, RD, mean kurtosis (MK), radial kurtosis (RK), and axial kurtosis (AK). The dipy implementation of DKI was used [139] and results can be found in the `qsirecon-DIPYDKI` directory.

Third, we fit the NODDI model[140] using the AMICO implementation.[141] A value of 1.7E-03 was used for parallel diffusivity and 3.0E-03 for isotropic diffusivity.[142] Intracellular volume fraction (ICVF), isotropic volume fraction (ISOVF), tissue fraction (1 - ISOVF), modulated ICVF, and Orientation Dispersion (OD) maps were also computed.[143]

Fourth, we used the Mean Apparent Propagator method (MAPMRI[144]), included in TORTOISE.[129] When fitting MAPMRI, we first fit a diffusion tensor using low *b*-value shells to determine the primary coordinate frame of the ensemble average diffusion propagator (EAP). This tensor fit can be considered the "inner shell" complementing the "full shell" tensor fit included in the `qsirecon-TORTOISE_model-tensor` results. Numerous scalar maps can be calculated from a MAPMRI fit, including the following return probabilities: Return to Origin Probability (RTOP), Return to Axis Probability (RTAP), and Return to Plane Probability (RTPP). General Non-Gaussianity (NG), Non-Gaussianity parallel (NGPar), and Non-Gaussianity Perpendicular (NGPer) to the primary direction were calculated. Propagator Anisotropy (PA), and Propagator Anisotropy theta (PAth) were also calculated.[144]

Finally, diffusion orientation distribution functions (ODFs) were reconstructed using generalized q-sampling imaging (GQI[145]) with a ratio of mean diffusion distance of 1.25 in DSI Studio (version 94b9c79). This method also describes more complicated diffusion dynamics without a model. Instead, it uses an analytic transform of the diffusion signal[145] to calculate water diffusion orientation distribution functions (dODFs), yielding scalar maps such as generalized fractional anisotropy (GFA), quantitative anisotropy (QA), MD, and isotropic component (ISO).[146]

To generate individual white matter bundles, we ran Automatic Tractography in DSI Studio (version 94b9c79) via the AutoTrack implementation. AutoTrack provides bundle shape statistics,[147] such as length, volume, surface area, endpoint surface area, endpoint radius, endpoint irregularity, overall curvature, and overall elongation. The average value of microstructural measures from each reconstruction model described above was also calculated for each bundle. In total, this process yielded 19 macrostructural and 64 microstructural metrics

ARTICLE IN PRESS

per bundle. We displayed individual white matter bundles that were reconstructed by DSI Studio using a custom Python script implementing features from dipy,[121] fury,[148] and pyAFQ.[149]

ASL image processing

We used ASLPrep v0.7.5[86,87] based on fMRIPrep[82–84] and Nipype v1.8.6,[89,90] to process ASL MRI data. Many internal operations of ASLPrep use Nilearn v0.11.1,[106] NumPy,[107] and SciPy.[109] For each ASL run, the following preprocessing was performed across all tasks and sessions. First, a reference volume was generated to use for head motion correction. Head-motion parameters were estimated for the ASL data using FSL's mcflirt.[96] Motion correction was performed separately for tagged and control volumes, in order to account for intensity differences between different contrasts, which can conflate intensity differences with head motion if the contrasts are motion-corrected together.[150] Next, we concatenated the motion parameters across volume types and re-calculated the relative root mean-squared deviation. The ASL reference was then co-registered to the T1w reference using bbregister (FreeSurfer) with six degrees of freedom. Notably, all resampling in ASLPrep concatenates all transformations so as to only interpolate the data once. Gridded (volumetric) resampling was performed using antsApplyTransforms, configured with Lanczos interpolation to minimize the smoothing effects of other kernels.[151]

Following preprocessing and as described in detail below, ASLPrep generates cerebral blood flow (CBF) maps using four different methods: standard CBF, SCORE-processed CBF (Structure Correlation based Outlier Rejection CBF), SCRUB CBF (Structural Correlation with RobUst Bayesian CBF), and BASIL CBF (Bayesian Interface for Arterial Spin Labeling CBF). First, standard CBF maps were calculated using a single-compartment general kinetic model.[152] Calibration (M0) volumes associated with the ASL scan were smoothed with a Gaussian kernel (FWHM = 5 mm) and the average calibration image was calculated and scaled by 10.0. Second, the Structural Correlation based Outlier Rejection (SCORE) algorithm was applied to the CBF time series to discard CBF volumes with outlying values[153] before computing the mean CBF. Third, we calculated CBF values using both the SCORE and the Structural Correlation with RobUst Bayesian (SCRUB) algorithm. SCRUB uses structural tissue probability maps to reweight the mean CBF;[153] note that the CBF time series used to calculate SCRUB CBF was cleaned using SCORE. Finally, CBF was also computed using Bayesian Inference for Arterial Spin Labeling (BASIL[154]), as implemented in FSL. BASIL computes CBF using a spatial regularization of the estimated perfusion image and additionally calculates a partial-volume corrected CBF image.[155]

For all CBF maps, we calculated the quality evaluation index (QEI[156]). QEI scores are based on the similarity between each CBF map and the structural images, the spatial variability of each CBF image, and the percentage of gray matter voxels containing negative CBF values. Parcellated CBF estimates were extracted for multiple atlases (as described below). Uncovered

ARTICLE IN PRESS

voxels were defined as those with values of all zeros or NaNs. Uncovered voxels were ignored when the parcel had more than 50.0% coverage, or the whole parcel was set to zero when the parcel had less than 50.0% coverage.

Atlases

The processed sMRI, fMRI, and ASL data include parcellated data from multiple atlases (**Figure S1**). FreeSurfer data (i.e., sMRI data) was parcellated using various atlases including Desikan Killiany,[157] Glasser,[158] Gordon,[159] Yeo,[160] Schaefer 200 through 1000,[117] and Brodmann areas.[161] fMRI data processed with XCP-D and ASL data processed using ASLPrep include parcellated data from many of the same atlases, including Schaefer, Gordon, and Glasser atlases. However, XCP-D and ASLPrep use the Schaefer Supplemented with Subcortical Structures (4S) atlas[117,158,162–164] at 10 different resolutions (156, 256, 356, 456, 556, 656, 756, 856, 956, and 1056 parcels) which combines the multi-resolution Schaefer parcellation with 56 subcortical parcels drawn from the CIT168 subcortical atlas,[162] Diedrichson cerebellar atlas,[163] HCP thalamic atlas,[164] and the amygdala and hippocampus parcels drawn from the HCP CIFTI subcortical parcellation.[158] XCP-D output also contains additional parcellated data from the Masonic Institute for the Developing Brain (MIDB) precision brain atlas[165] (thresholded at 75% probability), and the Tian subcortical atlas.[166]

ARTICLE IN PRESS

Data Records

Neuroimaging Data Structure and Organization

Raw neuroimaging data from this study are provided on OpenNeuro [accession number ds007116; https://openneuro.org/datasets/ds007116][44]. The original DICOM files were converted to NifTI format and structured to align with the Brain Imaging Data Structure (BIDS, version 1.8.0[81]) using HeuDiConv (version 1.3.2[167]). A custom heuristic file (available on this study's GitHub repository; see **Code Availability**) was generated to specify the organization of files and extract metadata from DICOMs. The extracted metadata was used to generate the JSON sidecars accompanying each NIfTI file in the BIDS dataset. As stipulated by BIDS, files were arranged into subject and session folders, with a `participants.tsv` file detailing demographic information, and an accompanying `sessions.tsv` file specifying relative acquisition times. Acquisition times were anonymized to prevent sharing protected health information such that the first scan date was set to the 15th of the original month in the year 1800. Subsequent sessions were adjusted accordingly such that the relative time intervals between sessions remained accurate, with times rounded to the nearest hour.

The raw neuroimaging dataset is available at OpenNeuro.[44] In addition to the TSV files described above, we include a `code/` folder which contains CuBIDS summary output files from

ARTICLE IN PRESS

every CuBIDS `apply` iteration we ran; a `derivatives/` folder which contains group-level task contrast outputs and outputs from running freesurfer-post; a `phenotype/` folder which contains JSON and TSV files corresponding to each cognitive task from the Penn CNB and each self-report survey; and a `sourcedata/` folder which contains the original MRI protocol document that was used at the scanner. The main folders of interest in the raw neuroimaging dataset are the sub-X and ses-X folders nested within each subject's folder. Each ses-X folder contains an `anat/` folder, which contains anatomical T1w, T2w, and MEGRE NIfTI and JSON files. The `dwi/` folder in each ses-X folder contains BVAL, BVEC, JSON, and NIfTI files from diffusion scans. The `fmap/` folder contains field maps for DWI and fMRI scans. The `func/` folder contains JSON, NIfTI, and events.tsv files for fMRI scans. Lastly, the `perf/` folder contains JSON and NIfTI files for ASL scans, as well as their corresponding reference m0 NIfTI and JSON files and the ASL context TSV file. Note that some sessions are missing one or more scans. Detailed information about the files included in the dataset is provided in **Table S2** and **Figure 3.**

In addition to the raw neuroimaging data, we provide analysis-ready processed derivatives on OpenNeuro. Each pipeline produced derivatives in BIDS format, along with HTML summaries of preprocessing steps. The outputs from freesurfer-post are included along with the raw neuroimaging data on OpenNeuro in the `derivatives/freesurfer-post/` folder [ds007116; https://openneuro.org/datasets/ds007116]. The participant-level and group-level task contrast maps from the *n*-back task are also included with the raw neuroimaging data on OpenNeuro in the `derivatives` folder [ds007116; https://openneuro.org/datasets/ds007116]. Group-level task contrast maps are also available on Neurovault [https://neurovault.org/collections/23717/]. For the rest of the processing pipelines, imaging derivatives from each BIDS App outputs are uploaded as separate datasets on OpenNeuro, as follows: [sMRIPrep: ds007089, https://openneuro.org/datasets/ds007089]; [fMRIprep: ds007088, https://openneuro.org/datasets/ds007088]; [XCP-D: ds007402, https://openneuro.org/datasets/ds007402]; [QSIPrep: ds007090, https://openneuro.org/datasets/ds007090]; [QSIRecon: ds007091, https://openneuro.org/datasets/ds007091]; [ASLPrep: ds006744, https://openneuro.org/datasets/ds006744].

Clinical Diagnostic and Phenotypic Data

Information about each participant's study group (e.g., PS, ADHD, or TD), determined from trained clinical assessors and confirmed by a clinical psychiatrist, is available on OpenNeuro[168] [accession number ds007116; https://openneuro.org/datasets/ds007116]. All diagnoses from the clinical interview are specified in the `participants.tsv` file. This file also includes demographic data such as participant age and sex.

ARTICLE IN PRESS

Cognitive assessment data from the Penn CNB results and self-report data are available under the `phenotype/` directory of the raw dataset on OpenNeuro [accession number ds007116; https://openneuro.org/datasets/ds007116]. Cognitive assessment data are provided as summary scores based on accuracy and reaction time. Self-report data are provided as raw responses with calculated summary scores for each session. Each Penn CNB task and self-report survey has a separate tsv file and an accompanying JSON file that describes the data represented in each column.

Technical Validation

Quality Control

Assessment of data quality is critically important for any neuroimaging study. Imaging artifacts, often due to in-scanner motion, can introduce bias in MRI measures.[169–176] Populations especially prone to higher in-scanner motion include youth[174,177–179] and those with psychiatric diagnoses[180] such as ADHD[181–183] and psychosis-spectrum disorders.[181,184,185] Furthermore, discrepancies in QC procedures employed by studies that use the same data can yield divergent results. For this data resource, we calculated multiple indices of image quality and in-scanner motion. Additionally, we provide recommended QC guidelines for each imaging modality, which are publicly shared on GitHub (https://github.com/PennLINC/transdiagnostic_executive_function/tree/main/QC/qc_csvs/final_QC_csvs). The total numbers of participants and sessions that passed QC based on our recommendations are summarized in **Figure 4** and further described in **Table 5.**

sMRI

For T1w structural scans, we provide manual QC ratings from trained raters. Manual ratings were assigned by two reviewers (B.L.S. & T.T.T.), who each rated four slices from each T1w scan in the dataset (two axial slices at z = 20 and z = 37 and two sagittal slices at x = -19 and x = 17) as a binary pass (1) or fail (0) based on visual examination. Following the independent ratings, the two reviewers compared their respective ratings for each individual slice and attempted to reach a consensus. For slices for which there remained a disagreement, a third expert manual rater (M.C.) determined the final rating. Once these final ratings were assigned, we calculated the average rating across all 4 slices for each scan, and used this average to make the final QC recommendation (0 = fail, 1 = pass, between 0 and 1 = artifact). After manual ratings, 86.5% of T1w sessions passed QC (**Figure 4; Table 5**).

In addition to these manual ratings, we provide left and right hemisphere Euler numbers, an automated numerical measure calculated by FreeSurfer[94,173] (**Figure 5a**). The Euler number quantifies the complexity of the surface topology of the reconstructed cortical surface, driven by the number of surface holes present. A value of 2 represents the maximum quality, whereas lower (including negative) values indicate lower quality. This measure has been validated by independent groups as a continuous measure of structural image quality.[29,169,173,186] As such, the

ARTICLE IN PRESS

Euler number provides an index of variation in data quality for images that pass manual QC and can be included as a model covariate in analyses.

DWI

For DWI scans, we provide QC recommendations based on measures of in-scanner motion and neighboring DWI correlation (NDC). After visual inspection of the scatterplot of mean FD against NDC, we excluded three scans with both high motion and low NDC (**Figure 5c)**. These scans were also excluded from our calculation of group-level scalar maps. After applying these criteria, 98.6% of DWI sessions passed QC (**Figure 4; Table 5**). In addition to the categorical QC labels, we recommend including FD and/or NDC as covariates in analyses of images that pass QC.

In addition to the global DWI QC, we provide specific QC ratings for white matter bundles reconstructed by tractometry. Specifically, we defined an 'outlier' bundle as any bundle whose total volume was greater than or equal to three standard deviations away from the mean total volume for that bundle across subjects and sessions. We summed the number of outliers for each subject and session: a subject/session with greater than 6 outlier bundles was considered an outlier subject/session and received a 'fail' rating.

fMRI

We used measures of in-scanner motion and field of view coverage for fMRI QC. Specifically, we used median FD[171] as a summary measure of head movement. After inspecting the distribution of median FD scores across all scans, we assigned 'pass' to any scan with median FD < 0.3 mm. In addition, we assessed the percent coverage for each cortical region in the Schaefer 1000 atlas with added subcortical regions.[117] Percent coverage was defined as the proportion of voxels remaining after preprocessing. Regions with <50% coverage were flagged. Subsequently, a scan was assigned a 'fail' rating if more than three regions were flagged for insufficient coverage. As such, all fMRI scans that received a final QC determination of 'pass' had median FD < 0.3 mm and three or fewer regions with insufficient coverage (**Figure 5b**). Based on this criteria, 94.4% of fMRI sessions passed QC (**Figure 4; Table 5**). We excluded scans that did not meet this criteria from group-level correlation matrices (excluded runs n = 71 across resting and n-back scans; **Figure 6**).

ASL

For ASL scans, we used QEI[156] as the main QC measure. QEI aggregates various features related to ASL image quality, including spatial similarity of the CBF map to the population-averaged template, the number of voxels with negative CBF values, and the signal-to-noise ratio. QEI values range from 0 to 1, where 1 represents the highest possible quality. Given the distribution of QEI values from our dataset, we assigned a 'pass' label to images with a QEI > 0.6 (**Figure 5d**). This threshold was determined based on previous literature classifying an example "average" scan from manual ratings to have a QEI = 0.68 and an example "poor" scan from manual ratings to have a QEI = 0.19.[187] Using this criteria, 81.2% of ASL sessions passed QC (**Figure 4; Table 5**).

ARTICLE IN PRESS

Neuroimaging Results

sMRI

We provide vertex-level sMRI data from FreeSurfer such as cortical thickness, curvature, and sulcal depth, as well as volumetric derivatives such as skull-stripped T1w images, tissue segmentations, brain masks, and the volume of subcortical regions. In addition, freesurfer-post produces atlas-based tabulated measures, including surface area of regions, surface vertices of regions, surface-based total gray matter volume, mean regional cortical thickness and standard deviation, mean curvature, average Gaussian curvature, and regional folding and curvature indices.[188] Finally, we include summary whole-brain metrics from multiple atlas parcellations, including the mean and standard deviation of the percentage of all vertices labeled as white and gray matter, ventricle size, cortical thickness, and surface area.

fMRI

Functional data derivatives include post-processed clean BOLD time series that are denoised, filtered, and censored; parcellated time series and functional connectivity matrices calculated from Pearson correlations; and ALFF and ReHo derivative maps. We created a group-level correlation matrix, computing the mean correlation across all subjects and sessions for both *n*-back and resting-state runs (**Figure 6a**). Each session is counted equally in the average; there was no participant-level averaging before generating the group-level matrix. The mean *n*-back and resting-state correlation matrices revealed canonical functional connectivity patterns, with stronger connectivity within previously described functional communities than between them.[117,160]

In addition to visualizing correlation matrices, we also averaged across every ALFF and ReHo map generated across multiple runs to provide group-level visualizations of ALFF[110] and ReHo[111] for resting-state functional MRI data (**Figure 6**). ALFF measures the intensity of BOLD signal fluctuations at each voxel, representing spontaneous neuronal activity at low frequencies. Group-level ALFF map shows a heterogeneous cortical distribution, with higher spontaneous activity in the prefrontal and occipital regions (**Figure 6b**). ReHo measures the local synchronization of a voxel's time series with its close neighbors. The group-level ReHo map shows generally high values, especially in association cortex (e.g., posterior cingulate and lateral parietal cortex; **Figure 6c**).

Task-contrast derivatives from running first and second-level analyses in Nilearn include both participant-level and group-level contrast maps for the 2-back > 0-back, 2-back > baseline, and 0-back > baseline contrasts. We include maps both with the RTDur regressor (visualized in **Figure 7**), and without the RTDur regressor in our data release. Note that our task design did not allow for robust estimation of baseline. Consistent with this limitation, the 2-back > baseline and

ARTICLE IN PRESS

0-back > baseline contrasts showed unexpected deactivations across various modeling strategies (**Figure S2**).

For the fractal *n*-back working memory task at the group level, the 2-back > 0-back contrast demonstrates increased activation in regions commonly associated with working memory and executive function, including frontoparietal cortical areas (**Figure 7a**), consistent with the extensive prior literature.[189,190] To evaluate the robustness and consistency of these group-level 2-back > 0-back contrast results, we also compared our results to those from a similar fractal *n*-back task administered as part of the Philadelphia Neurodevelopmental Cohort (PNC[116]). This revealed that the 2-back > 0-back maps between the two studies were highly similar (**Figure 7b;** r=0.924, p_{spin}=0.0001).

DWI

We release derived DWI measures including white matter bundles, bundle-level metrics, and scalar maps from multiple models including traditional tensor-based models, DKI, NODDI, MAPMRI, and GQI. Exemplar group-average maps from one metric per model are displayed in **Figure 8**. From the QSIRecon outputs using the tensor model in DSI Studio, we display the group-level FA map (**Figure 8a**). Similarly, from the GQI model in DSI Studio, we generated group-level GFA maps (**Figure 8b**). As expected, both mean FA and GFA maps showed canonical patterns,[191–193] with maximal values in white matter due to anisotropic diffusion, and lower values in gray matter due to isotropic diffusion. Furthermore, from the DKI model, we generated group-level MK maps that quantify the average degree of non-Gaussian water diffusion, demonstrating expected patterns of higher MK in white matter, and lower values in gray matter[137–139,194,195] (**Figure 8e**). We used NODDI model outputs from QSIRecon[196] to generate group-level ICVF maps, providing an estimate of neurite density within each voxel (**Figure 8c**). The group-level ICVF map demonstrated canonical patterns consistent with previous work,[196–198] with higher neurite density in white matter and lower density in gray matter. From the MAPMRI model, we display a group-average RTAP, which quantifies the probability that water molecules return to their original axis (i.e., parallel to the primary diffusion axis). The group-level RTAP map displayed consistent patterns with previous literature,[144,198,199] with higher RTAP values in white matter and lower values in gray matter (**Figure 8d**).

We also include individual-specific white matter bundles in the data release. In addition to providing the bundles themselves, we release bundle shape statistics as well as the mean value from each scalar metric across all models. Together, this rich data facilitates analysis of person-specific white matter anatomy. Reconstructed white matter bundles (the arcuate fasciculus, corticospinal tract, and inferior fronto-occipital fasciculus) are displayed for two exemplar participants (sub-20188 and sub-20712) across all three longitudinal sessions (**Figure 9**).

ASL

ARTICLE IN PRESS

ASL derivatives include standard CBF maps, SCORE-processed CBF, SCRUB CBF, BASIL CBF, and BASIL CBF with partial volume correction. The mean CBF maps for some of these methods is displayed in **Figure 10.** CBF maps are consistent with expected patterns of regional cerebral perfusion,[200,201] with higher CBF in gray matter and lower CBF in white matter.

Usage Notes

Transdiagnostic cognitive, clinical, and multimodal imaging data are critical for investigating EF deficits in adolescents and understanding how those deficits contribute to diverse psychopathology. The Penn LEAD dataset includes longitudinal curated clinical diagnostic, cognitive, and multimodal neuroimaging data from 132 participants. Participants include adolescents diagnosed with ADHD and PS disorders as well as typically developing individuals. We publicly provide raw, anonymized data in BIDS format[44] for sMRI, fMRI, DWI, ASL, and MEGRE for QSM scans, allowing researchers to process the data through their own pipelines. In addition to the raw data, we provide sMRI[202], resting-state and task fMRI[203,204], DWI[205,206], and ASL data[207] derivatives that are fully-processed through BIDS Apps. Processed task fMRI data includes participant and group-level *n*-back task contrast maps. These derived measures – alongside corresponding detailed QC information – ensure that Penn LEAD can immediately be used for hypothesis testing.

Data Availability

All raw neuroimaging data, behavioral and imaging derivative data from the *n*-back task, phenotypic data, and freesurfer-post outputs are available on OpenNeuro [accession number: ds007116[44]; https://openneuro.org/datasets/ds007116]. The raw data also includes output files from the CuBIDS software in the `code/` folder, and the MRI protocol PDF in the `sourcedata/` folder.

Analysis-ready data is also provided on OpenNeuro for sMRIPrep[202] [accession number: ds007089; https://openneuro.org/datasets/ds007089], fMRIPrep[203] [accession number: ds007088; https://openneuro.org/datasets/ds007088], XCP-D[204] [accession number: ds007402; https://openneuro.org/datasets/ds007402], QSIPrep[205] [accession number: ds007090; https://openneuro.org/datasets/ds007090], QSIRecon[206] [accession number: ds007091; https://openneuro.org/datasets/ds007091], and ASLPrep[207] [accession number: ds006744; https://openneuro.org/datasets/ds006744]. Group-level task contrast maps from the *n*-back task are also available on Neurovault [https://neurovault.org/collections/23717/], in addition to the derivatives folder of the OpenNeuro dataset above [accession number: ds007116; https://openneuro.org/datasets/ds007116]. Quality control recommendations for each imaging modality are available on GitHub [https://github.com/PennLINC/transdiagnostic_executive_function/tree/main/QC/qc_csvs/final_QC_csvs].

ARTICLE IN PRESS

Funding

This work was supported by grant R01MH113550 from the National Institute of Mental Health: Additional support was provided by NIH R37MH125829, R01MH112847, Penn-CHOP Lifespan Brain Institute, AI2D Center, and the AE Foundation. G.S. was supported by a postdoctoral fellowship from the Canadian Institutes of Health Research (CIHR). K.M. was supported by The Air Force Office of Scientific Research Grant FA9550-22-1-0337 and NIH Grant T32MH126036.

Author Contributions

K.M., S.L., and L.B. contributed to data collection. B.L.S., M.C., S.L.M., T.S., S.P.S., and T.T.T. contributed to data curation. B.L.S., G.S., M.C., S.L.M., T.S., S.P.S., and T.T.T. contributed to analysis. T.D.S. and D.B. acquired funding. T.D.S. provided supervision. B.L.S., G.S., S.P.S., and T.S. contributed to visualization. B.L.S, G.S., and T.D.S. wrote the original draft, and all authors contributed to review and editing of the final draft.

Competing Interests

All authors declare no known competing financial or other interests that could have influenced the work reported in this paper.

ARTICLE IN PRESS

ARTICLE IN PRESS

Figures

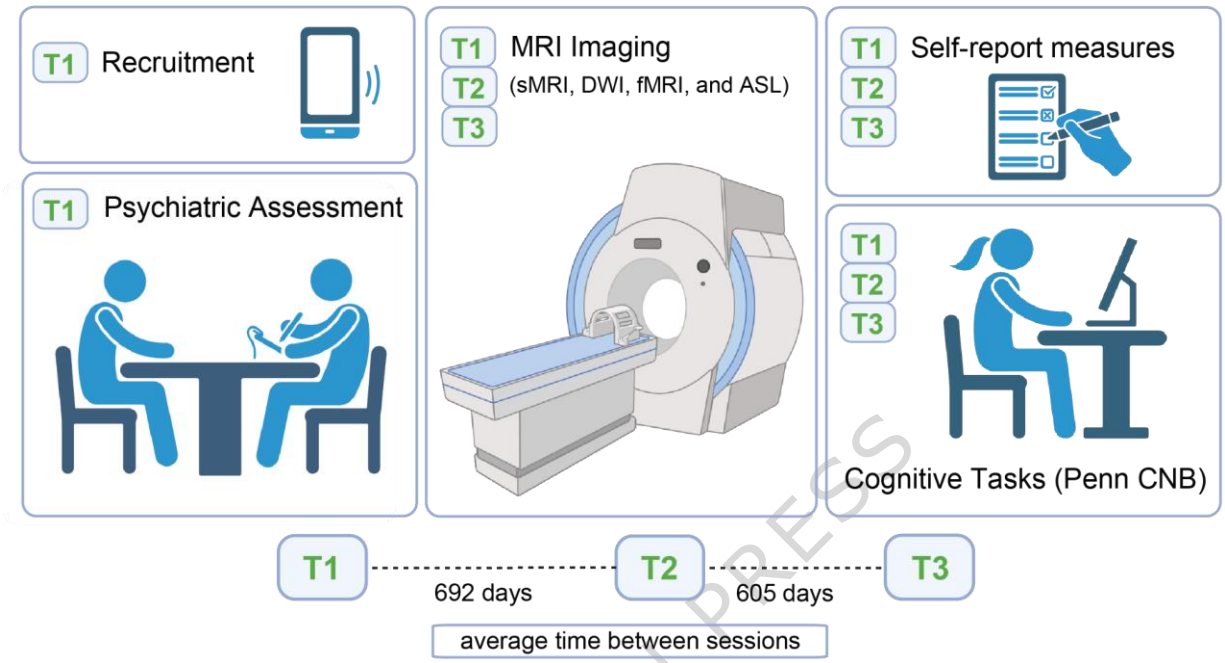


Figure 1. Overview of recruitment and visits. At Timepoint 1 (T1), participants were recruited from the Children's Hospital of Philadelphia, then were placed into 'ADHD,' 'Psychosis Spectrum (PS),' or 'Typically Developing' study groups following psychiatric assessment via a detailed clinical interview. At T1, in addition to any subsequent longitudinal timepoints (T2 and T3), participants completed magnetic resonance imaging (MRI) scanning sessions, self-report assessments, and the Penn Computerized Neurocognitive Battery (Penn CNB). sMRI = structural MRI; DWI = diffusion-weighted MRI; fMRI = functional MRI; ASL = arterial spin labeling. Created in BioRender. Sevchik, B. (2025) https://BioRender.com/ern7vq6

ARTICLE IN PRESS

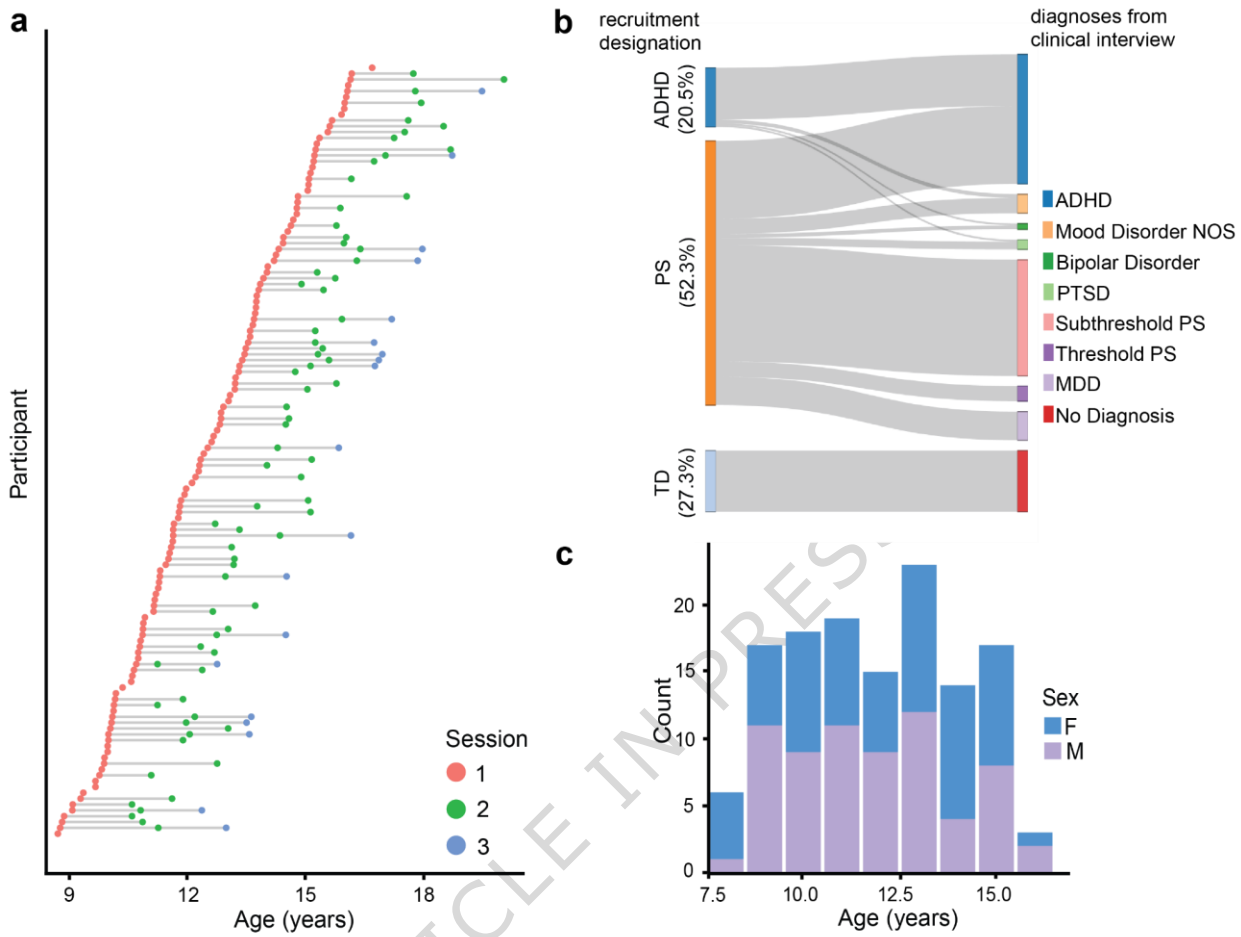


Figure 2. Participant demographics and clinical diagnostic summary. (a) Longitudinal data is represented as a feather plot, where each individual dot represents an individual session. Line lengths between sessions are proportional to the time elapsed between sessions for each participant. **(b)** Clinical diagnostic summary data are visualized using a Sankey plot. Values on the left side of the Sankey plot correspond to the percentage of unique participants in each pre-determined recruitment group out of all participants in the dataset, according to clinical interviews (ADHD = attention-deficit hyperactivity disorder; PS = psychosis-spectrum (including threshold and subthreshold); TD = typically developing). Rectangles on the right of the plot correspond to the percentage of unique participants who met diagnostic criteria for each disorder according to clinical interviews (including additional, more detailed co-morbid diagnoses beyond diagnoses indicated by recruitment groups) out of the total sample: ADHD: 51.5%; Mood Disorder Not Otherwise Specified (Mood Disorder NOS): 7.6%; Bipolar disorder: 2.3%; Post-traumatic stress disorder (PTSD): 3.8%; Subthreshold Psychosis Spectrum (PS; clinical high risk for psychosis): 46.2%; Threshold Psychosis Spectrum (PS): 6.1%; Major depressive disorder (MDD): 11.4%; No clinical psychiatric diagnosis (No Diagnosis): 27.3%. Gray lines from the left to the right of the Sankey plot are proportional to the amount of participants from each recruitment group contributing to the total percentage of participants with each disorder. **(c)** The distribution of the age at intake and sex of the sample: Female: 49.2%; Average age at intake: 11.9 years old.

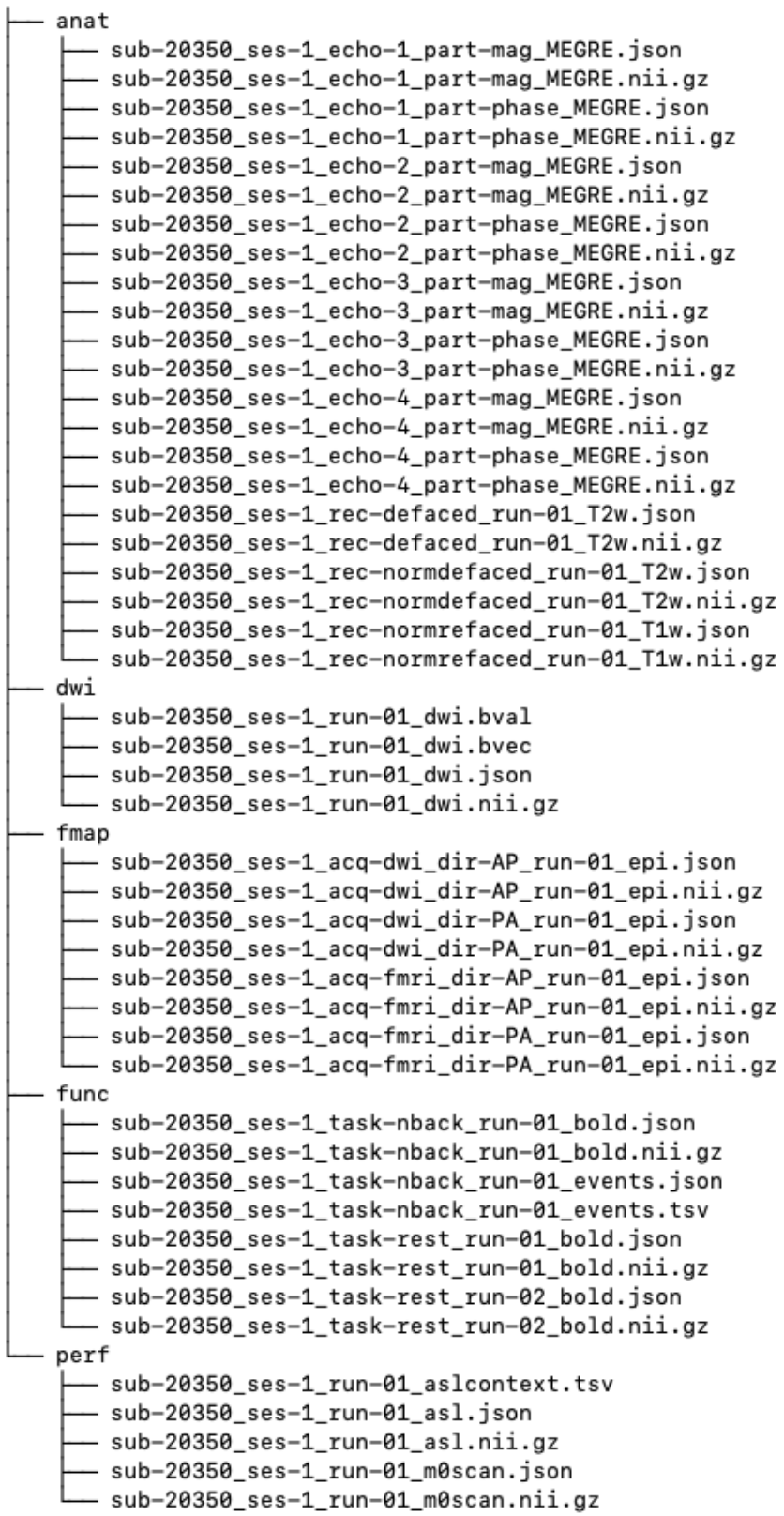


Figure 3. Exemplar subject directory structure. The figure above shows an example folder structure in BIDS format for one session in one subject (sub-20350, ses-1).

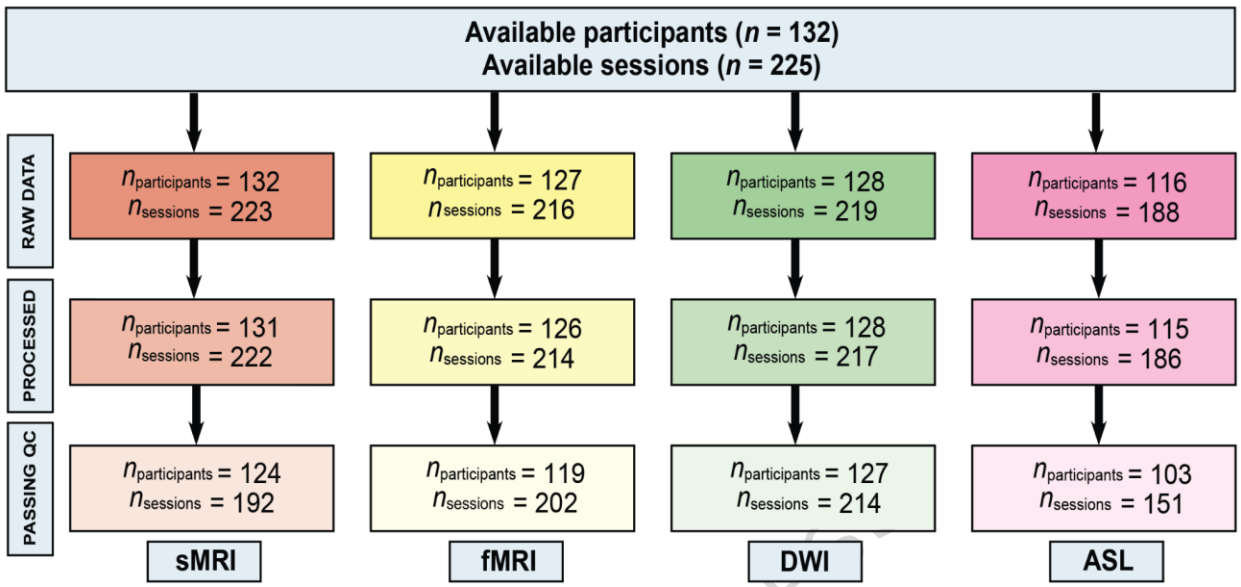


Figure 4. Preprocessing and quality control workflow. The workflow demonstrates the number of participants and scans/sessions from the original collected data that survived preprocessing and met our QC recommendations (i.e., data with "pass" QC).

ARTICLE IN PRESS

ARTICLE IN PRESS

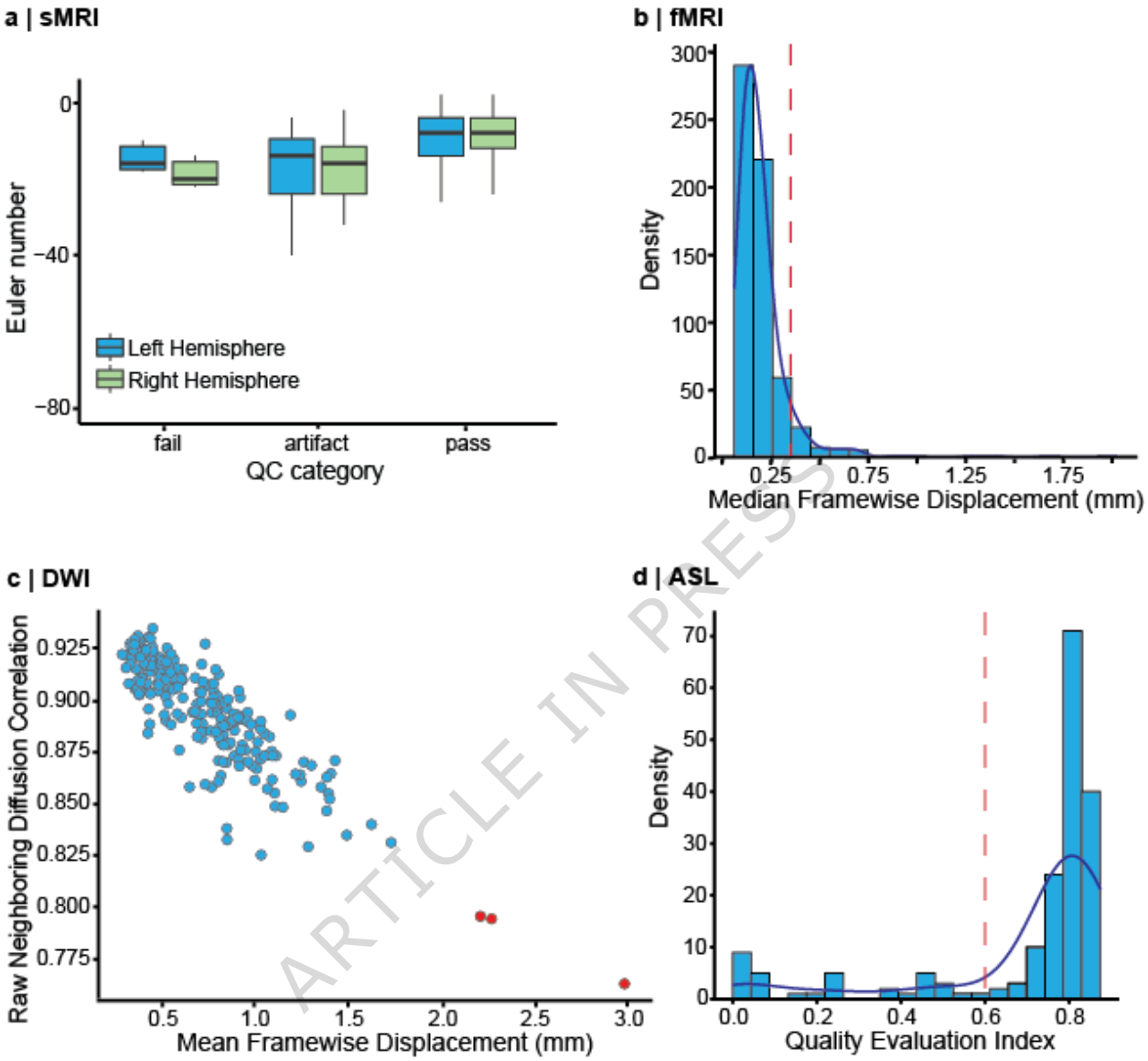


Figure 5. Neuroimaging data quality control. (a) Automated image quality measures (i.e., Euler number) along with manual ratings were used to assess the quality of sMRI data. Distribution of left and right hemisphere Euler numbers are visualized using box plots. The Euler number is an automated numerical measure calculated by FreeSurfer and provides a continuous estimate of sMRI data quality. Box plots are grouped according to categorical quality ratings assigned from manual review of T1w scans. Boxes represent the interquartile range of the distribution, where the middle line in each box represents the median Euler number. **(b)** Median FD was used as a measure of fMRI data quality, reflecting participants' in-scanner motion. Distribution of median framewise displacement (FD) across all functional scans is plotted as a histogram. The red dashed line corresponds to our recommended threshold to consider an fMRI scan of adequate quality ("Pass" label: median FD < 0.3 mm). **(c)** Mean framewise displacement (FD) and raw neighboring DWI correlation (NDC) were used to assess diffusion-weighted imaging (DWI) data quality. Each dot in the scatter plot represents a DWI scan. Red dots indicate 'outliers' with low NDC and high motion (i.e., Mean FD > 2.0 mm; NDC < 0.8) that did not "pass" quality control per our recommendations. **(d)** Quality Evaluation Index (QEI) was

ARTICLE IN PRESS

used as a measure of ASL data quality. Distribution of QEI across all ASL scans is plotted as a histogram. The red dashed line corresponds to our recommended threshold to consider an ASL scan of adequate quality ("Pass" label: QEI > 0.6).

ARTICLE IN PRESS

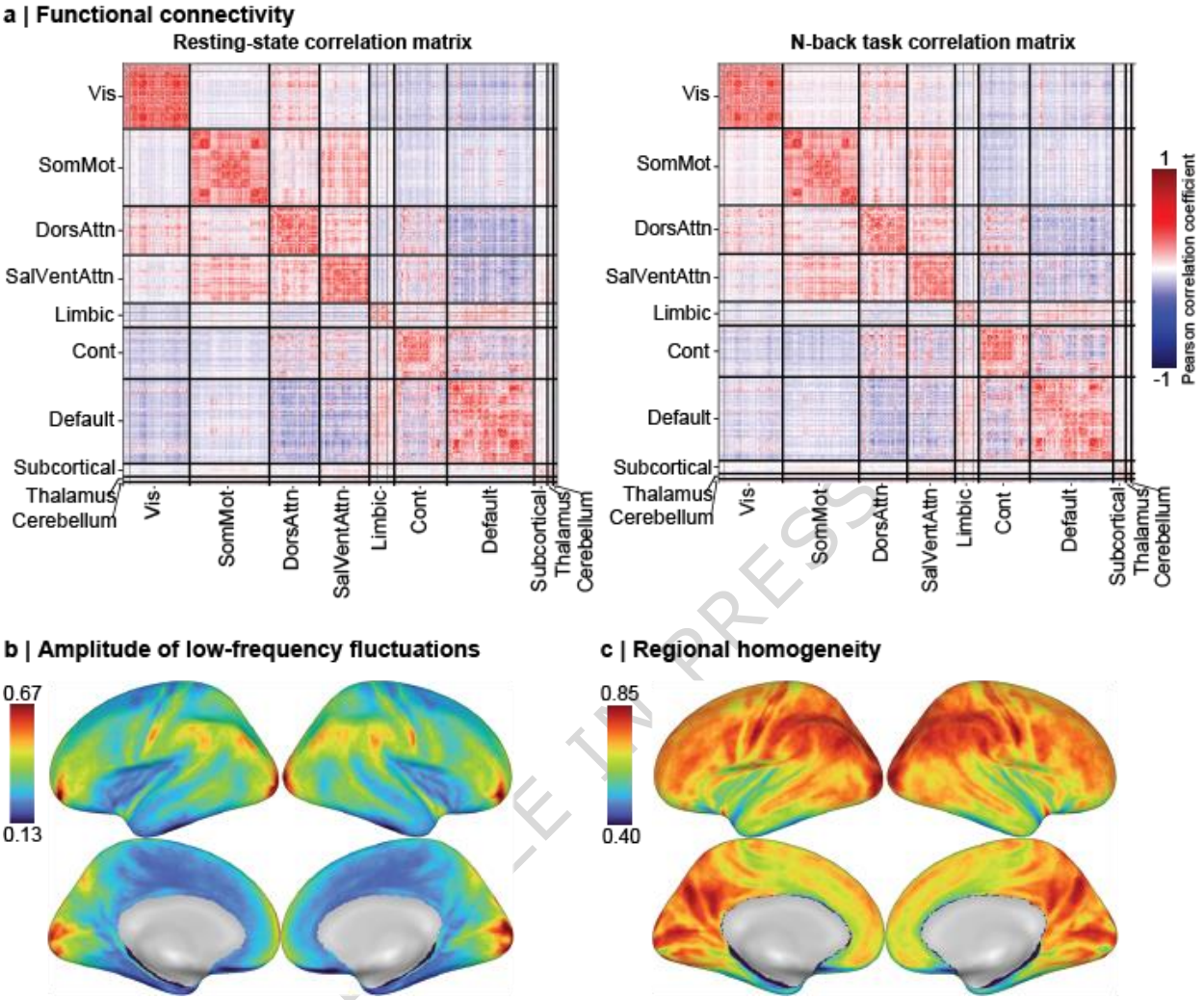


Figure 6. Functional neuroimaging correlation matrices and surface plots. (a) Group-level correlation matrices for the resting-state scans and fractal *n*-back task scans, parcellated from the Schaefer 1000 atlas with additional subcortical regions appended and quantified using a Pearson correlation coefficient, revealed canonical functional connectivity patterns and intrinsic networks. Parcels with poor coverage (<50% coverage in more than 3 scans, *n* excluded parcels = 9) across many subjects and sessions were shown as missing values in the group-level correlation matrices. **(b)** Group-level amplitude of low-frequency fluctuations (ALFF) map showed a heterogeneous cortical distribution, with stronger activity in occipital and prefrontal regions. **(c)** Group-level regional homogeneity (ReHo) map showed strong regional coherence of neural activity across the cortex.

ARTICLE IN PRESS

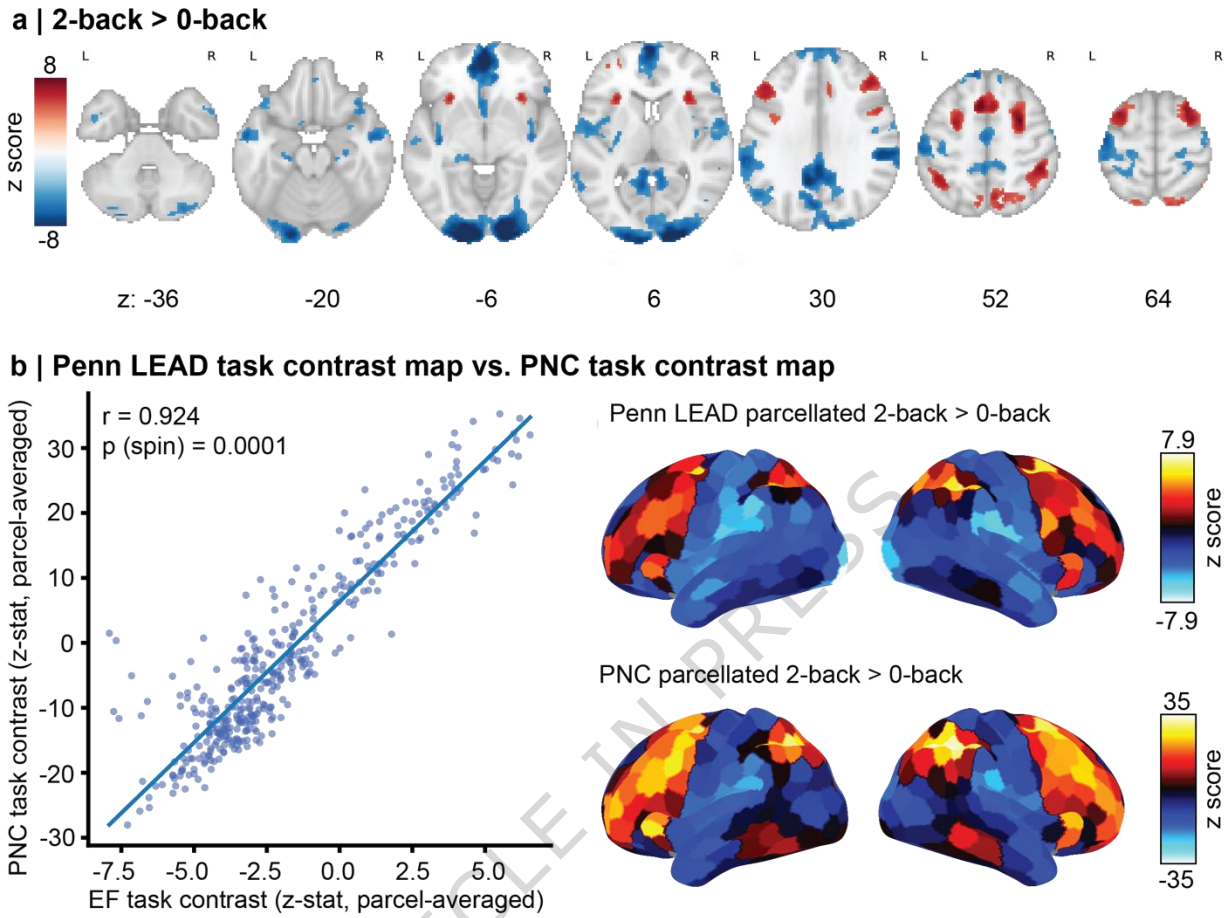


Figure 7. fMRI activation maps from *n*-back task. (a) Group-level z-statistic maps for the 2-back > 0-back task contrast from a second-level non-parametric permutation test (10,000 permutations), thresholded at voxelwise FWE-corrected $p < 0.05$ (two-sided; cluster-forming threshold $p < 0.001$). **(b)** The relationship between Penn LEAD and Philadelphia Neurodevelopmental Cohort (PNC) z-statistic maps is shown in a scatter plot for the same contrast (left). Both maps were projected to the fsLR surface and parcellated into 400 cortical regions using the Schaefer 400 atlas (right). The statistical significance of the Pearson correlation was assessed using a spin-based permutation test (10,000 permutations). Unthresholded second-level maps were used for the parcellated visualizations and correlation between Penn LEAD and PNC maps.

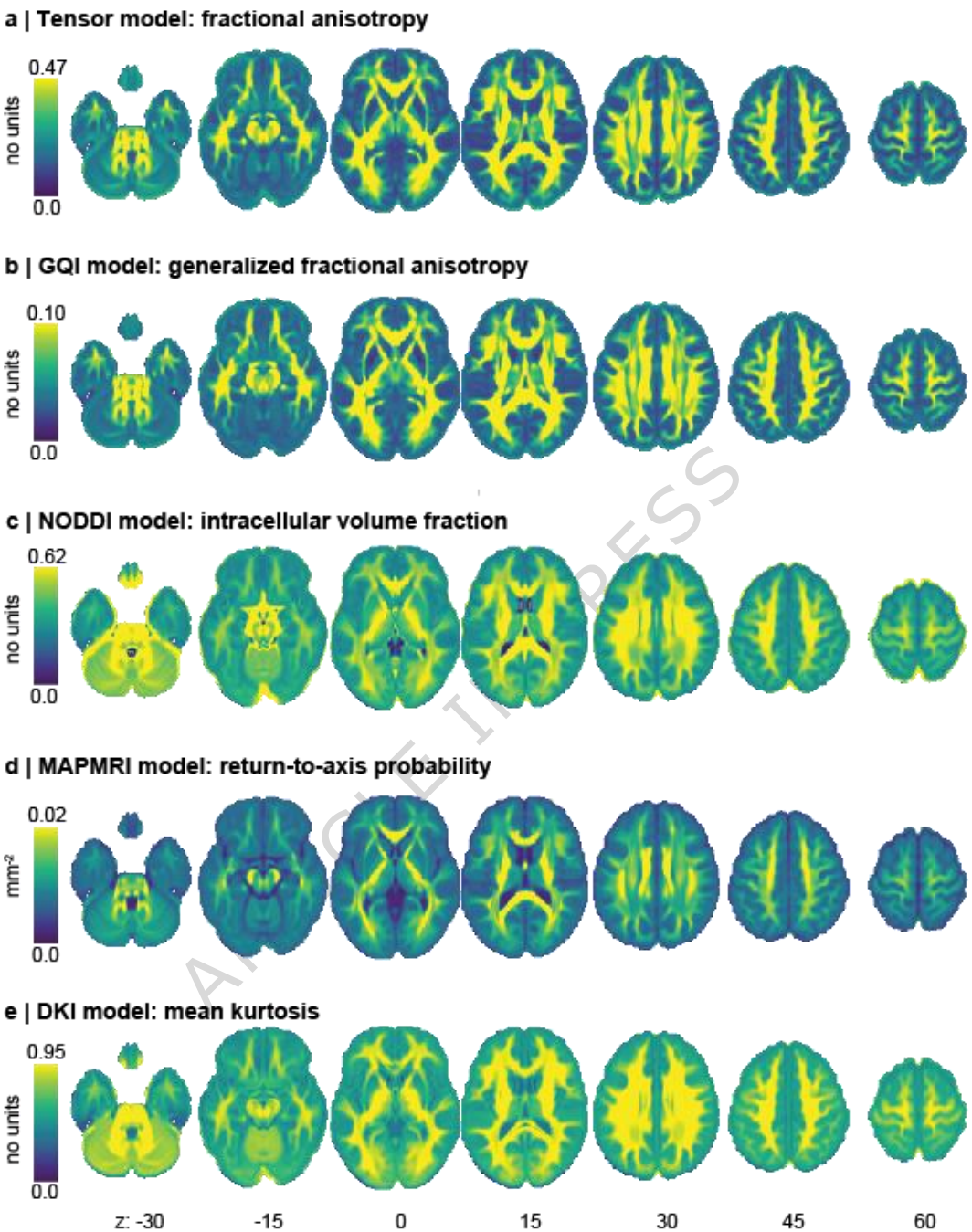


Figure 8. DWI scalar maps. The Penn LEAD dataset provides various DWI scalar maps from QSIRecon. Example group-level maps are shown for four measures: **(a)** Fractional anisotropy from the tensor model in DSI Studio; **(b)** Generalized fractional anisotropy (GFA) from the GQI model in DSI Studio; **(c)** Intracellular volume fraction (ICVF) from the NODDI model; **(d)** Return-to-axis probability (RTAP) from the MAPMRI model with TORTOISE; and **(e)** Mean kurtosis from the DKI model. All axial slices are shown at MNI z-coordinates -30, -15, 0, 15, 30, 45, and 60, overlaid on the MNI152NLin2009cAsym template space.

ARTICLE IN PRESS

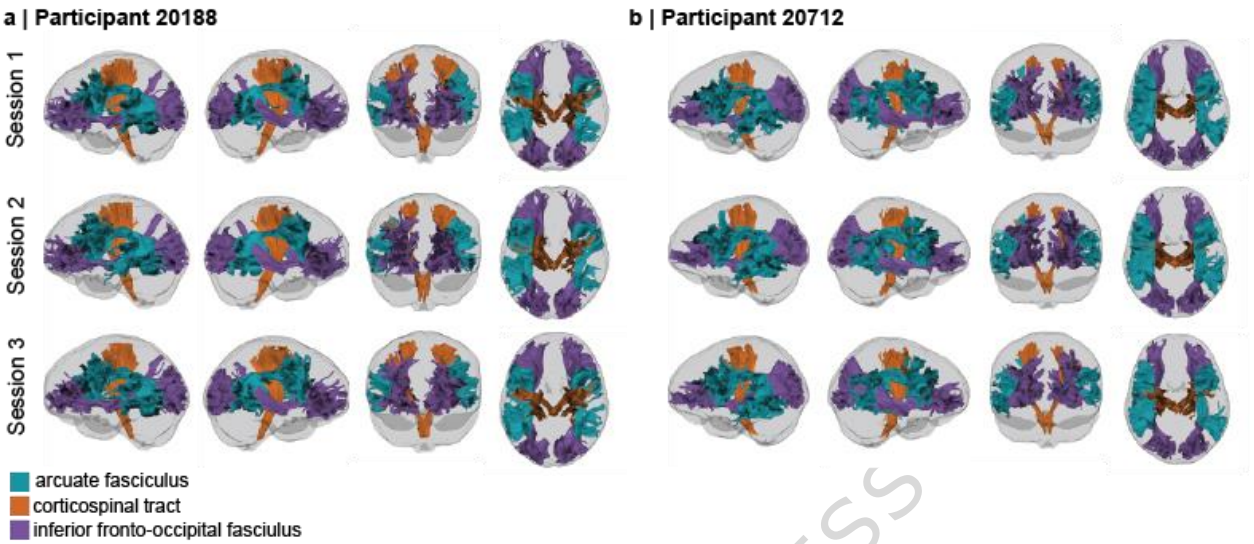


Figure 9. DWI reconstructed tracts. The Penn LEAD dataset also provides individual-level reconstructed diffusion bundles. Reconstructed bundles are shown for two example individuals across all three longitudinal sessions: **(a)** participant 20188 and **(b)** participant 20712. Displayed example bundles are the association arcuate fasciculus (green), projection brainstem corticospinal tract (orange), and association inferior fronto-occipital fasciculus (purple).

ARTICLE IN PRESS

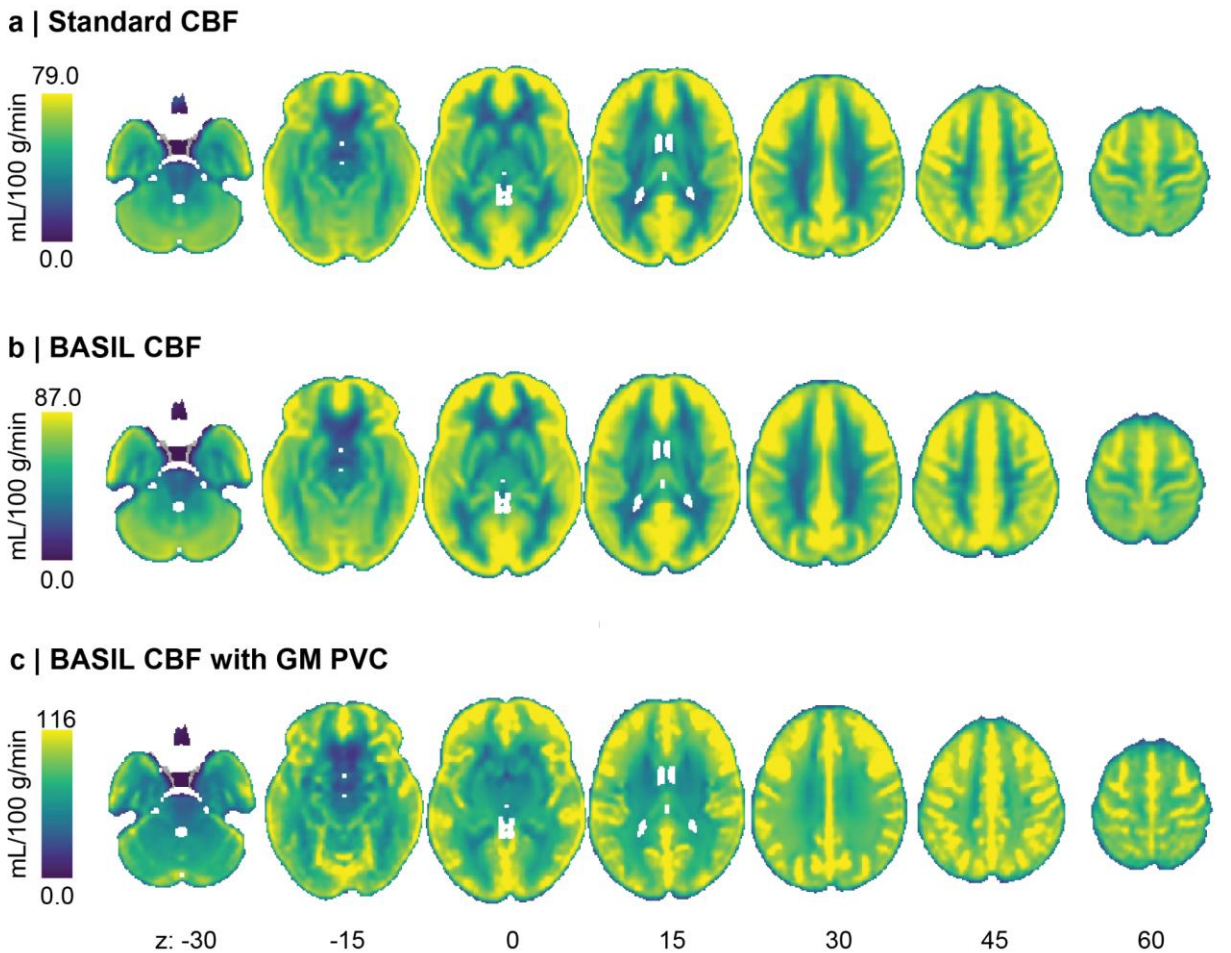


Figure 10. ASL CBF maps. The Penn LEAD dataset provides various measures of cerebral blood flow (CBF) from ASLPrep. Example group-level CBF maps are highlighted for three different measures: **(a)** Standard CBF; **(b)** BASIL estimation of CBF; and **(c)** BASIL CBF estimated with partial volume correction (PVC) for a gray-matter specific map. All axial slices are shown at MNI z-coordinates -30, -15, 0, 15, 30, 45, and 60, overlaid on the MNI152NLin6Asym template.

ARTICLE IN PRESS

Tables

Study group	ADHD	Subthreshold PS	Threshold PS	Mood Disorder NOS	Bipolar Disorder	PTSD	MDD
ADHD (n = 27)	27 (100%)	0 (0.0%)	0 (0.0%)	2 (7.4%)	1 (3.7%)	1 (3.7%)	0 (0.0%)
PS (n = 69)	41 (59.4%)	61 (88.4%)	8 (11.6%)	8 (11.6%)	2 (2.9%)	4 (5.8%)	15 (21.7%)
TD/NC (n = 36)	0 (0.0%)	0 (0.0%)	0 (0.0%)	0 (0.0%)	0 (0.0%)	0 (0.0%)	0 (0.0%)

Table 1. Summary of diagnoses within each recruitment group. Participants in the ADHD and PS recruitment groups had various other co-morbid diagnoses. Note that for recruitment purposes, any participant with co-morbid ADHD and PS were included in the PS recruitment group, which explains the 0.0% co-morbidity of subthreshold PS and threshold PS in the ADHD recruitment group. ADHD = attention-deficit hyperactivity disorder; PS = psychosis-spectrum (including threshold and subthreshold); TD = typically developing.

ARTICLE IN PRESS

ARTICLE IN PRESS

CNB Task	Battery	Cognitive Domain	Citation
Penn Abstraction, Inhibition and Working Memory Task	EF	Executive function	Moore et al., 2023; Glahn et al., 2000
Penn Face Memory Test	LiBI	Episodic memory	Moore et al., 2015, 2023; Gur et al., 2010, 2012; Scott et al., 2020
Children's Penn Word Memory Test	LiBI	Episodic memory	Moore et al., 2015, 2023; Gur et al., 2010, 2012
Short Computerized Finger-Tapping Task	LiBI	Sensorimotor speed	Gur et al., 2010, 2012; Scott et al., 2020
Penn Emotion Recognition Task for Children	LiBI	Social cognition	Moore et al., 2015, 2023; Gur et al., 2010, 2012
Digit Symbol Test	EF	Executive function	Scott et al., 2020; Moore et al., 2023
Short Letter-*N*-Back (2-back)	LiBI	Executive function	Moore et al., 2015; Gur et al., 2010; Gur et al., 2012
Measured Emotion Differentiation Test	LiBI	Social cognition	Moore et al., 2015; Gur et al., 2012; Moore et al., 2023
Motor Praxis Test	LiBI	Sensorimotor speed	Gur et al., 2012; Scott et al., 2020
Penn Conditional Exclusion Task for Children	LiBI	Executive function	Moore et al., 2015; Gur et al., 2010, 2012; Scott et al., 2020
Short Penn Continuous Performance Test-Number and Letter Version	LiBI	Executive function	Moore et al., 2015, 2023; Gur et al., 2010, 2012; Scott et al, 2020
Penn Matrix Reasoning Test	LiBI	Complex cognition	Moore et al., 2015, 2023; Gur et al., 2012; Scott et al., 2020
Variable Short Penn Line Orientation Test	LiBI	Complex cognition	Moore et al., 2015, 2023; Gur et al., 2010, 2012; Scott et al., 2020
Children's Verbal Reasoning Test	LiBI	Complex cognition	Moore et al., 2015, 2023; Gur et al., 2010, 2012
Short Visual Object Learning Test	LiBI	Episodic memory	Moore et al., 2015, 2023; Gur et al., 2010, 2012; Scott et al., 2020
Trailmaking A	EF	Executive function	Scott et al., 2020
Trailmaking B	EF	Executive function	Scott et al., 2020
Effort Discounting Task	EF	Reward	Moore et al., 2023
Delayed Discounting Task	EF	Reward	Moore et al., 2023
Risk Discounting Task	EF	Reward	Moore et al., 2023

ARTICLE IN PRESS

Age Differentiation Test	LiBI	Social cognition	Moore et al., 2015, 2023; Gur et al., 2012

Table 2. Overview of cognitive tasks in the dataset from the Penn CNB. The table above summarizes the cognitive domains corresponding to the tasks included in batteries from the Penn Computerized Neurocognitive Battery that we included in our dataset. Detailed descriptions of each task can be found in the papers cited for each task.

ARTICLE IN PRESS

ARTICLE IN PRESS

Self-Report Scale	Battery	Measures	Citation
Adverse Life Experiences Scale (ALES)	main	Occurrence and developmental timing of adverse childhood experiences	Hawes et al., 2021
Affective Lability Scale (ALS-18)	main	Affective lability (aspect of emotion dysregulation)	Contardi et al., 2018
Affective Reactivity Index (ARI)	main	Irritability	Stringaris et al., 2012
Altman Self-Rating Mania Scale (ASRM)	main	Mania	Altman et al., 1997
Beck Depression Inventory (BDI-1A)	main	Depression	Beck, 1961
Behavioral Inhibition/Activation System (BIS-BAS)	main	Motivational systems underlying behavior and affect	Carver & White, 1994
Extended Strengths and Weaknesses Assessment of ADHD Symptoms and Normal Behavior (E-SWAN ADHD)	main	ADHD symptoms	Alexander et al., 2020; Swanson et al., 2012
Extended Strengths and Weaknesses Assessment of DMDD Symptoms and Normal Behavior - DMDD (E-SWAN DMDD)	main	DMDD symptoms	Alexander et al., 2020
The Motivation and Pleasure Scale - Self-Report (MAP-SR)	main	Severity of negative symptoms	Llerena et al., 2013
Positive and Negative Affect Schedule (PANAS)	main	Positive and negative affect (mood)	Watson et al., 1988
PROMIS Pediatric Anxiety (PPA)	main	Anxiety symptoms	Irwin et al., 2012
PRIME Screen (Self-Report)	main	Subthreshold psychosis symptoms	Kobayashi et al., 2008, Calkins et al. 2025
Revised Physical Anhedonia Scale (RPAS)	main	Physical anhedonia symptoms	Chapman et al., 1976
Revised Social Anhedonia Scale (RSAS)	main	Social anhedonia symptoms	Chapman et al., 1976
Substance Use Questionnaire	main	Substance use	Han et al., 1999
Tanner Developmental Scale - Boy	main	Pubertal changes in boys	Marshall & Tanner, 1970
Tanner Developmental Scale - Girl	main	Pubertal changes in girls	Marshall & Tanner, 1969
Wolf Intrinsic Motivation/Extrinsic Motivation (Wolf IM/EM)	main	Trait intrinsic and extrinsic motivation	Didier et al., 2023
State-Trait Anxiety Inventory (state)	pre-scan post-scan	State anxiety	Spielberger et al., 1983
State-Trait Anxiety Inventory (trait)	pre-scan	Trait anxiety	Spielberger et al., 1983

Table 3. Overview of self-report scales in the dataset. The table above summarizes the self-report scales collected, along with the symptom or trait they are designed to measure. The full STAI was administered before the scan as part of the pre-scan battery, and just the state anxiety items of the STAI were administered after the scan as part of the post-

ARTICLE IN PRESS

scan battery. All other scales were administered as part of the main battery at each session. Details about each scale can be found in the papers cited for each scale.

ARTICLE IN PRESS

ARTICLE IN PRESS

Sequence	Slices	% FOV phase	Resolution (mm)	TR (ms)	TE (ms)	TI (ms)	Flip Angle (degree)	Multi Band Accel	Phase Partial Fourier
T1w	176	100%	1.0x1.0x1.0	2500	2.9	1070	8	n/a	1.0
T2w	176	100%	1.0x1.0x1.0	3200	565	n/a	120	n/a	1.0
DWI	81	100%	1.7x1.7x1.7	4200	89	n/a	90	3	0.75
DWI fmap PA	81	100%	1.7x1.7x1.7	12400	89	n/a	90	n/a	0.75
DWI fmap AP	81	100%	1.7x1.7x1.7	12400	89	n/a	90	n/a	0.75
Resting-state fMRI	60	100%	2.4x2.4x2.4	800	30	n/a	52	6	1.0
n-back task fMRI	60	100%	2.4x2.4x2.4	800	30	n/a	52	6	1.0
fMRI fmap PA	60	100%	2.4x2.4x2.4	7030	80	n/a	90	n/a	1.0
fMRI fmap AP	60	100%	2.4x2.4x2.4	7030	80	n/a	90	n/a	1.0
ASL	32	100%	3.75x3.75x3.75	4298	10	n/a	90	n/a	1.0
MEGRE	96	100%	1.5x1.5x1.5	35	7.5, 15, 22.5, 30	n/a	15	n/a	1.0

Table 4. Neuroimaging acquisition parameters.

ARTICLE IN PRESS

ARTICLE IN PRESS

Modality	Exclusion Criteria	N sessions (%) passed
sMRI	Manual rating of “fail” (due to ringing, etc. in visual image slices)	192 (86.5%)
fMRI	Median FD > 0.3 or more than 3 regions with incomplete coverage	202 (94.4%)
DWI	Mean FD > 2.0 or neighborhood corr < 0.8	214 (98.6%)
ASL	QEI <= 0.6	151 (81.2%)

Table 5. Summary of QC exclusion criteria for each imaging modality. Note that for sMRI, there were not two binary options, but three options: “pass”, “artifact”, or “fail”. “Artifacts” are not included in the N sessions that passed QC. For DWI scans, the criteria are based on the calculations of mean FD and NDC from scalar maps, not from bundle-level outliers.

ARTICLE IN PRESS

ARTICLE IN PRESS

Code Availability

We used open-source, containerized, reproducible processing pipelines and software for all imaging processing and analysis. HeuDiConv was used to convert images from DICOM to BIDS format [code here: https://github.com/nipy/heudiconv; documentation here: https://heudiconv.readthedocs.io/en/latest/].[167] CuBIDS software was used to facilitate curation of BIDS images [code here: https://github.com/PennLINC/CuBIDS; documentation here: https://cubids.readthedocs.io/en/latest/].[78] BIDS-App Bootstrap (BABS) software was used to preprocess images by wrapping around BIDS Apps [code here: https://github.com/PennLINC/babs; documentation here: https://pennlinc-babs.readthedocs.io/en/stable/].[88] The custom configuration YAML files used with BABS can be found on GitHub here: https://github.com/PennLINC/transdiagnostic_executive_function/tree/main/preprocessing/babs_yaml_files.

The following BIDS Apps were used: fMRIPrep [code here: https://github.com/nipreps/fmriprep; documentation here: https://fmriprep.org/en/stable/; Docker Hub link here: https://hub.docker.com/layers/nipreps/fmriprep/25.0.0/images/sha256-04555ac849ec9e08fa8c70ebf0e0eb6fc99fd54b589c4108b5309de7dca0194b],[82–84] XCP-D [code here: https://github.com/PennLINC/xcp_d; documentation here: https://xcp-d.readthedocs.io/en/latest/; Docker Hub link here: https://hub.docker.com/layers/pennlinc/xcp_d/0.10.7/images/sha256-fa10fe96b9ed1cb63322cfebc7dff8a21b7dcca84487b977c06be3d2c863f33a],[98] QSIPrep [code here: https://github.com/PennLINC/qsiprep; documentation here: https://qsiprep.readthedocs.io/en/latest/; Docker Hub link here: https://hub.docker.com/layers/pennlinc/qsiprep/1.0.0/images/sha256-ebbfe74b9d35df9fbe9873d383a5f11171b0411ae9a9098d330290884c7c853b],[85] QSIRecon [code here: https://github.com/PennLINC/qsirecon; documentation here: https://qsirecon.readthedocs.io/en/latest/; Docker Hub link here: https://hub.docker.com/layers/pennlinc/qsirecon/1.1.0/images/sha256-4450a0f93cbafe8c3d3840c366f1ae3866bcf86ba2ac1114140810ed162b1326],[85] freesurfer-post [code here: https://github.com/PennLINC/freesurfer-post; Docker Hub link here: https://hub.docker.com/layers/pennlinc/freesurfer-post/0.1.2/images/sha256-73821e8c1dd4e078e8879f91fcccb760465ca71e52e8cecf99252ac31e1f74bc], and ASLPrep[86,87] [code here: https://github.com/PennLINC/aslprep; documentation here: https://aslprep.readthedocs.io/en/latest/; Docker Hub link here: https://hub.docker.com/layers/pennlinc/aslprep/0.7.5/images/sha256-1cc832ac1bfdc2f6bec126c84bc9bdb8b8cb6dc2995f58d5d3aaaca04f4a99ba].

For task contrast analyses, we used Nilearn[114] [code here: https://github.com/nilearn/nilearn; documentation here: https://nilearn.github.io/stable/index.html]. All custom code for data organization, quality control, self-report scoring, group-level analyses, and figure generation is available and

ARTICLE IN PRESS

described in detail on GitHub here:
https://github.com/PennLINC/transdiagnostic_executive_function.

ARTICLE IN PRESS

ARTICLE IN PRESS

References

1. Ferguson, H. J., Brunsdon, V. E. A. & Bradford, E. E. F. The developmental trajectories of executive function from adolescence to old age. *Sci. Rep.* **11**, 1382 (2021).
2. Luna, B., Padmanabhan, A. & O'Hearn, K. What has fMRI told us about the Development of Cognitive Control through Adolescence? *Brain Cogn.* **72**, 101–113 (2010).
3. Tervo-Clemmens, B. *et al.* A canonical trajectory of executive function maturation from adolescence to adulthood. *Nat. Commun.* **14**, 6922 (2023).
4. Powers, A. & Casey, B. J. The Adolescent Brain and the Emergence and Peak of Psychopathology. *J. Infant Child Adolesc. Psychother.* **14**, 3–15 (2015).
5. Romer, A. L. & Pizzagalli, D. A. Is executive dysfunction a risk marker or consequence of psychopathology? A test of executive function as a prospective predictor and outcome of general psychopathology in the adolescent brain cognitive development study®. *Dev. Cogn. Neurosci.* **51**, 100994 (2021).
6. Shroff, D. M. *et al.* Predictors of executive function trajectories in adolescents with and without ADHD: Links with academic outcomes. *Dev. Psychopathol.* **36**, 1489–1502 (2024).
7. Snyder, H. R., Friedman, N. P. & Hankin, B. L. Transdiagnostic Mechanisms of Psychopathology in Youth: Executive Functions, Dependent Stress, and Rumination. *Cogn. Ther. Res.* **43**, 834–851 (2019).
8. Barkley, R. A. Behavioral inhibition, sustained attention, and executive functions: Constructing a unifying theory of ADHD. *Psychol. Bull.* **121**, 65–94 (1997).
9. Forbes, N. F., Carrick, L. A., McIntosh, A. M. & Lawrie, S. M. Working memory in schizophrenia: a meta-analysis. *Psychol. Med.* **39**, 889–905 (2009).
10. Fusar-Poli, P. *et al.* Cognitive Functioning in Prodromal Psychosis: A Meta-analysis. *Arch. Gen. Psychiatry* **69**, (2012).

ARTICLE IN PRESS

ARTICLE IN PRESS

11. De Wilde, A., Koot, H. M. & Van Lier, P. A. C. Developmental Links Between Children's Working Memory and their Social Relations with Teachers and Peers in the Early School Years. *J. Abnorm. Child Psychol.* **44**, 19–30 (2016).
12. Irwin, L. N. *et al.* Activities of daily living and working memory in pediatric attention-deficit/hyperactivity disorder (ADHD). *Child Neuropsychol.* **27**, 468–490 (2021).
13. Morgan, P. L. *et al.* Executive function deficits in kindergarten predict repeated academic difficulties across elementary school. *Early Child. Res. Q.* **46**, 20–32 (2019).
14. Rohlf, H. L., Holl, A. K., Kirsch, F., Krahé, B. & Elsner, B. Longitudinal Links between Executive Function, Anger, and Aggression in Middle Childhood. *Front. Behav. Neurosci.* **12**, 27 (2018).
15. Shanmugan, S. *et al.* Common and Dissociable Mechanisms of Executive System Dysfunction Across Psychiatric Disorders in Youth. *Am. J. Psychiatry* **173**, 517–526 (2016).
16. Jacobson, L. A., Williford, A. P. & Pianta, R. C. The role of executive function in children's competent adjustment to middle school. *Child Neuropsychol.* **17**, 255–280 (2011).
17. Nowrangi, M. A., Lyketsos, C., Rao, V. & Munro, C. A. Systematic Review of Neuroimaging Correlates of Executive Functioning: Converging Evidence From Different Clinical Populations. *J. Neuropsychiatry Clin. Neurosci.* **26**, 114–125 (2014).
18. Eng, C. M. *et al.* Longitudinal investigation of executive function development employing task-based, teacher reports, and fNIRS multimethodology in 4- to 5-year-old children. *Dev. Sci.* **25**, e13328 (2022).
19. Hirota, T., McElroy, E., Fujiwara, T. & Boden, J. Editorial: Longitudinal data analysis in child and adolescent mental health. *Front. Psychiatry* **13**, 1038190 (2022).
20. Best, J. R. & Miller, P. H. A developmental perspective on executive function. *Child Dev.* **81**, 1641–1660 (2010).
21. Fan, X.-R. *et al.* A longitudinal resource for population neuroscience of school-age children and adolescents in China. *Sci. Data* **10**, 545 (2023).

ARTICLE IN PRESS

22. Somerville, L. H. *et al.* The Lifespan Human Connectome Project in Development: A large-scale study of brain connectivity development in 5–21 year olds. *NeuroImage* **183**, 456–468 (2018).
23. Evans, A. C. The NIH MRI study of normal brain development. *NeuroImage* **30**, 184–202 (2006).
24. Biswal, B. B. *et al.* Toward discovery science of human brain function. *Proc. Natl. Acad. Sci.* **107**, 4734–4739 (2010).
25. Consortium, T. The ADHD-200 Consortium: a model to advance the translational potential of neuroimaging in clinical neuroscience. *Front. Syst. Neurosci.* **6**, (2012).
26. Alexander, L. M. *et al.* An open resource for transdiagnostic research in pediatric mental health and learning disorders. *Sci. Data* **4**, 170181 (2017).
27. Addington, J. *et al.* North American Prodrome Longitudinal Study (NAPLS 3): Methods and baseline description. *Schizophr. Res.* **243**, 262–267 (2022).
28. Nigg, J. T. *et al.* The Oregon ADHD-1000: A new longitudinal data resource enriched for clinical cases and multiple levels of analysis. *Dev. Cogn. Neurosci.* **60**, 101222 (2023).
29. Shafiei, G. *et al.* Reproducible Brain Charts: An open data resource for mapping brain development and its associations with mental health. Preprint at https://doi.org/10.1101/2025.02.24.639850 (2025).
30. Karcher, N. R. & Barch, D. M. The ABCD study: understanding the development of risk for mental and physical health outcomes. *Neuropsychopharmacology* **46**, 131–142 (2021).
31. Volkow, N. D. *et al.* The conception of the ABCD study: From substance use to a broad NIH collaboration. *Dev. Cogn. Neurosci.* **32**, 4–7 (2018).
32. Nooner, K. B. *et al.* The NKI-Rockland Sample: A Model for Accelerating the Pace of Discovery Science in Psychiatry. *Front. Neurosci.* **6**, (2012).
33. Tobe, R. H. *et al.* A longitudinal resource for studying connectome development and its psychiatric associations during childhood. *Sci. Data* **9**, 300 (2022).

ARTICLE IN PRESS

ARTICLE IN PRESS

34. Schumann, G. *et al.* The IMAGEN study: reinforcement-related behaviour in normal brain function and psychopathology. *Mol. Psychiatry* **15**, 1128–1139 (2010).

35. Di Martino, A. *et al.* The autism brain imaging data exchange: towards a large-scale evaluation of the intrinsic brain architecture in autism. *Mol. Psychiatry* **19**, 659–667 (2014).

36. Jwa, A. S. & Poldrack, R. A. The spectrum of data sharing policies in neuroimaging data repositories. *Hum. Brain Mapp.* **43**, 2707–2721 (2022).

37. Laird, A. R. Large, open datasets for human connectomics research: Considerations for reproducible and responsible data use. *NeuroImage* **244**, 118579 (2021).

38. Milham, M. P. *et al.* Assessment of the impact of shared brain imaging data on the scientific literature. *Nat. Commun.* **9**, 2818 (2018).

39. Tedersoo, L. *et al.* Data sharing practices and data availability upon request differ across scientific disciplines. *Sci. Data* **8**, 192 (2021).

40. White, T., Blok, E. & Calhoun, V. D. Data sharing and privacy issues in neuroimaging research: Opportunities, obstacles, challenges, and monsters under the bed. *Hum. Brain Mapp.* **43**, 278–291 (2022).

41. Zuo, X.-N. *et al.* An open science resource for establishing reliability and reproducibility in functional connectomics. *Sci. Data* **1**, 140049 (2014).

42. Wagner, A. S. *et al.* FAIRly big: A framework for computationally reproducible processing of large-scale data. *Sci. Data* **9**, 80 (2022).

43. Halchenko, Y. *et al.* DataLad: distributed system for joint management of code, data, and their relationship. *J. Open Source Softw.* **6**, 3262 (2021).

44. Sevchik, B.L. *et al.* Penn LEAD: Penn Longitudinal Executive functioning in Adolescent Development. OpenNeuro. [Dataset]. https://doi.org/10.18112/openneuro.ds007116.v1.0.6 (2026).

45. Calkins, M. E. *et al.* The Philadelphia Neurodevelopmental Cohort: constructing a deep phenotyping collaborative. *J. Child Psychol. Psychiatry* **56**, 1356–1369 (2015).

ARTICLE IN PRESS

ARTICLE IN PRESS

46. Kaufman, J. *et al.* Schedule for Affective Disorders and Schizophrenia for School-Age Children-Present and Lifetime Version (K-SADS-PL): Initial Reliability and Validity Data. *J. Am. Acad. Child Adolesc. Psychiatry* **36**, 980–988 (1997).

47. Calkins, M. E. *et al.* Persistence of psychosis spectrum symptoms in the Philadelphia Neurodevelopmental Cohort: a prospective two-year follow-up. *World Psychiatry* **16**, 62–76 (2017).

48. Miller, T. J. *et al.* Prodromal Assessment With the Structured Interview for Prodromal Syndromes and the Scale of Prodromal Symptoms: Predictive Validity, Interrater Reliability, and Training to Reliability. *Schizophr. Bull.* **29**, 703–715 (2003).

49. Gur, R. C. *et al.* A cognitive neuroscience-based computerized battery for efficient measurement of individual differences: Standardization and initial construct validation. *J. Neurosci. Methods* **187**, 254–262 (2010).

50. Gur, R. C. *et al.* Age group and sex differences in performance on a computerized neurocognitive battery in children age 8−21. *Neuropsychology* **26**, 251–265 (2012).

51. Moore, T. M., Reise, S. P., Gur, R. E., Hakonarson, H. & Gur, R. C. Psychometric properties of the Penn Computerized Neurocognitive Battery. *Neuropsychology* **29**, 235–246 (2015).

52. Moore, T. M. *et al.* Construction of a computerized adaptive test (CAT-CCNB) for efficient neurocognitive and clinical psychopathology assessment. *J. Neurosci. Methods* **386**, 109795 (2023).

53. Scott, J. C. *et al.* Development of a computerised neurocognitive battery for children and adolescents with HIV in Botswana: study design and protocol for the Ntemoga study. *BMJ Open* **10**, e041099 (2020).

54. Glahn, D. C., Cannon, T. D., Gur, R. E., Ragland, J. D. & Gur, R. C. Working memory constrains abstraction in schizophrenia. *Biol. Psychiatry* **47**, 34–42 (2000).

55. Halchenko, Y. *et al.* con/open-brain-consent: 1.2.0. Zenodo https://doi.org/10.5281/ZENODO.7106031 (2022).

ARTICLE IN PRESS

ARTICLE IN PRESS

56. Hawes, D. J. *et al.* Capturing the developmental timing of adverse childhood experiences: The Adverse Life Experiences Scale. *Am. Psychol.* **76**, 253–267 (2021).
57. Contardi, A., Imperatori, C., Amati, I., Balsamo, M. & Innamorati, M. Assessment of Affect Lability: Psychometric Properties of the ALS-18. *Front. Psychol.* **9**, 427 (2018).
58. Stringaris, A. *et al.* The Affective Reactivity Index: a concise irritability scale for clinical and research settings. *J. Child Psychol. Psychiatry* **53**, 1109–1117 (2012).
59. Altman, E. G., Hedeker, D., Peterson, J. L. & Davis, J. M. The Altman Self-Rating Mania Scale. *Biol. Psychiatry* **42**, 948–955 (1997).
60. Beck, A. T. An Inventory for Measuring Depression. *Arch. Gen. Psychiatry* **4**, 561 (1961).
61. Carver, C. S. & White, T. L. Behavioral inhibition, behavioral activation, and affective responses to impending reward and punishment: The BIS/BAS Scales. *J. Pers. Soc. Psychol.* **67**, 319–333 (1994).
62. Muris, P., Meesters, C., De Kanter, E. & Timmerman, P. E. Behavioural inhibition and behavioural activation system scales for children: relationships with Eysenck's personality traits and psychopathological symptoms. *Personal. Individ. Differ.* **38**, 831–841 (2005).
63. Alexander, L. M., Salum, G. A., Swanson, J. M. & Milham, M. P. Extended Strengths and Weaknesses Assessment of Normal Behavior. https://doi.org/10.1037/t74737-000 (2020).
64. Swanson, J. M. *et al.* Categorical and Dimensional Definitions and Evaluations of Symptoms of ADHD: History of the SNAP and the SWAN Rating Scales. *Int. J. Educ. Psychol. Assess.* **10**, 51–70 (2012).
65. Llerena, K. *et al.* The Motivation and Pleasure Scale–Self-Report (MAP-SR): Reliability and validity of a self-report measure of negative symptoms. *Compr. Psychiatry* **54**, 568–574 (2013).
66. Watson, D., Clark, L. A. & Tellegen, A. Development and validation of brief measures of positive and negative affect: The PANAS scales. *J. Pers. Soc. Psychol.* **54**, 1063–1070 (1988).
67. Irwin, D. E. *et al.* Development of six PROMIS pediatrics proxy-report item banks. *Health Qual. Life Outcomes* **10**, 22 (2012).

ARTICLE IN PRESS

68. Calkins, M. E. *et al.* Development and Validation of a Brief Age-Normed Screening Tool for Subthreshold Psychosis Symptoms in Youth. *Schizophr. Bull.* **51**, 1242–1253 (2025).

69. Kobayashi, H. *et al.* A self-reported instrument for prodromal symptoms of psychosis: Testing the clinical validity of the PRIME Screen—Revised (PS-R) in a Japanese population. *Schizophr. Res.* **106**, 356–362 (2008).

70. Chapman, L. J., Chapman, J. P. & Raulin, M. L. Scales for physical and social anhedonia. *J. Abnorm. Psychol.* **85**, 374–382 (1976).

71. Han, C., Mcgue, M. K. & Iacono, W. G. Lifetime tobacco, alcohol and other substance use in adolescent Minnesota twins: univariate and multivariate behavioral genetic analyses. *Addiction* **94**, 981–993 (1999).

72. Marshall, W. A. & Tanner, J. M. Variations in the Pattern of Pubertal Changes in Boys. *Arch. Dis. Child.* **45**, 13–23 (1970).

73. Marshall, W. A. & Tanner, J. M. Variations in pattern of pubertal changes in girls. *Arch. Dis. Child.* **44**, 291–303 (1969).

74. Didier, P. R. *et al.* Evaluation of a new intrinsic and extrinsic motivation scale in youth with psychosis spectrum symptoms. *Compr. Psychiatry* **127**, 152413 (2023).

75. Spielberger, C., Gorsuch, R., Lushene, R., Vagg, P. & Jacobs, G. Manual for the State-Trait Anxiety Inventory (Form Y1 - Y2). (1983).

76. Ragland, J. D. *et al.* Working Memory for Complex Figures: An fMRI Comparison of Letter and Fractal n-Back Tasks. (2015).

77. Satterthwaite, T. D. *et al.* Functional Maturation of the Executive System during Adolescence. *J. Neurosci.* **33**, 16249–16261 (2013).

78. Covitz, S. *et al.* Curation of BIDS (CuBIDS): A workflow and software package for streamlining reproducible curation of large BIDS datasets. *NeuroImage* **263**, 119609 (2022).

79. Cox, R. W. AFNI: Software for Analysis and Visualization of Functional Magnetic Resonance Neuroimages. *Comput. Biomed. Res.* **29**, 162–173 (1996).

ARTICLE IN PRESS

80. Gulban, O. F. *et al.* poldracklab/pydeface: PyDeface v2.0.2. Zenodo https://doi.org/10.5281/ZENODO.6856482 (2022).

81. Gorgolewski, K. J. *et al.* The brain imaging data structure, a format for organizing and describing outputs of neuroimaging experiments. *Sci. Data* **3**, 160044 (2016).

82. Esteban, O. *et al.* fMRIPrep: a robust preprocessing pipeline for functional MRI. *Nat. Methods* **16**, 111–116 (2019).

83. Esteban, O. *et al.* Analysis of task-based functional MRI data preprocessed with fMRIPrep. *Nat. Protoc.* **15**, 2186–2202 (2020).

84. Markiewicz, C. J. *et al.* fMRIPrep: a robust preprocessing pipeline for functional MRI. Zenodo https://doi.org/10.5281/ZENODO.15085876 (2025).

85. Cieslak, M. *et al.* QSIPrep: an integrative platform for preprocessing and reconstructing diffusion MRI data. *Nat. Methods* **18**, 775–778 (2021).

86. Adebimpe, A. *et al.* ASLPrep: a platform for processing of arterial spin labeled MRI and quantification of regional brain perfusion. *Nat. Methods* **19**, 683–686 (2022).

87. Adebimpe, A. *et al.* ASLPrep (Version 0.7.5). Zenodo https://doi.org/https://doi.org/10.5281/zenodo.3759082 (2023).

88. Zhao, C. *et al.* A reproducible and generalizable software workflow for analysis of large-scale neuroimaging data collections using BIDS Apps. *Imaging Neurosci.* **2**, imag–2–00074 (2024).

89. Gorgolewski, K. *et al.* Nipype: A Flexible, Lightweight and Extensible Neuroimaging Data Processing Framework in Python. *Front. Neuroinformatics* **5**, (2011).

90. Esteban, O. *et al.* nipy/nipype: 1.9.2. Zenodo https://doi.org/10.5281/ZENODO.15054171 (2025).

91. Tustison, N. J. *et al.* N4ITK: Improved N3 Bias Correction. *IEEE Trans. Med. Imaging* **29**, 1310–1320 (2010).

92. Avants, B., Tustison, N. J. & Song, G. Advanced Normalization Tools: V1.0. *Insight J.* https://doi.org/10.54294/uvnhin (2009) doi:10.54294/uvnhin.

ARTICLE IN PRESS

ARTICLE IN PRESS

93. Zhang, Y., Brady, M. & Smith, S. Segmentation of brain MR images through a hidden Markov random field model and the expectation-maximization algorithm. *IEEE Trans. Med. Imaging* **20**, 45–57 (2001).

94. Dale, A. M., Fischl, B. & Sereno, M. I. Cortical Surface-Based Analysis. *NeuroImage* **9**, 179–194 (1999).

95. Glasser, M. F. *et al.* The minimal preprocessing pipelines for the Human Connectome Project. *NeuroImage* **80**, 105–124 (2013).

96. Jenkinson, M., Bannister, P., Brady, M. & Smith, S. Improved Optimization for the Robust and Accurate Linear Registration and Motion Correction of Brain Images. *NeuroImage* **17**, 825–841 (2002).

97. Glasser, M. F. *et al.* The minimal preprocessing pipelines for the Human Connectome Project. *NeuroImage* **80**, 105–124 (2013).

98. Mehta, K. *et al.* XCP-D: A Robust Pipeline for the post-processing of fMRI data.

99. Ciric, R. *et al.* Benchmarking of participant-level confound regression strategies for the control of motion artifact in studies of functional connectivity. *NeuroImage* **154**, 174–187 (2017).

100. Satterthwaite, T. D. *et al.* An improved framework for confound regression and filtering for control of motion artifact in the preprocessing of resting-state functional connectivity data. *NeuroImage* **64**, 240–256 (2013).

101. Cox, R. W. & Hyde, J. S. Software tools for analysis and visualization of fMRI data. *NMR Biomed.* **10**, 171–178 (1997).

102. Marcus, D. S. *et al.* Informatics and Data Mining Tools and Strategies for the Human Connectome Project. *Front. Neuroinformatics* **5**, (2011).

103. Ciric, R. *et al.* TemplateFlow: FAIR-sharing of multi-scale, multi-species brain models. *Nat. Methods* **19**, 1568–1571 (2022).

104. Hunter, J. D. Matplotlib: A 2D Graphics Environment. *Comput. Sci. Eng.* **9**, 90–95 (2007).

105. Brett, M. *et al.* nipy/nibabel: 5.3.1. Zenodo https://doi.org/10.5281/ZENODO.13936989 (2024).

ARTICLE IN PRESS

ARTICLE IN PRESS

106. Abraham, A. *et al.* Machine learning for neuroimaging with scikit-learn. *Front. Neuroinformatics* **8**, (2014).

107. Harris, C. R. *et al.* Array programming with NumPy. *Nature* **585**, 357–362 (2020).

108. Yarkoni, T. *et al.* PyBIDS: Python tools for BIDS datasets. *J. Open Source Softw.* **4**, 1294 (2019).

109. Virtanen, P. *et al.* SciPy 1.0: fundamental algorithms for scientific computing in Python. *Nat. Methods* **17**, 261–272 (2020).

110. Zou, Q.-H. *et al.* An improved approach to detection of amplitude of low-frequency fluctuation (ALFF) for resting-state fMRI: Fractional ALFF. *J. Neurosci. Methods* **172**, 137–141 (2008).

111. Jiang, L. & Zuo, X.-N. Regional Homogeneity: A Multimodal, Multiscale Neuroimaging Marker of the Human Connectome. *The Neuroscientist* **22**, 486–505 (2016).

112. Zhang, B. *et al.* Surface-based regional homogeneity in bipolar disorder: A resting-state fMRI study. *Psychiatry Res.* **278**, 199–204 (2019).

113. Taylor, P. A. & Saad, Z. S. FATCAT: (An Efficient) Functional And Tractographic Connectivity Analysis Toolbox. *Brain Connect.* **3**, 523–535 (2013).

114. Nilearn contributors *et al.* nilearn. Zenodo https://doi.org/10.5281/ZENODO.8397156 (2025).

115. Mumford, J. A. *et al.* The response time paradox in functional magnetic resonance imaging analyses. *Nat. Hum. Behav.* **8**, 349–360 (2023).

116. Satterthwaite, T. D. *et al.* The Philadelphia Neurodevelopmental Cohort: A publicly available resource for the study of normal and abnormal brain development in youth. *NeuroImage* **124**, 1115–1119 (2016).

117. Schaefer, A. *et al.* Local-Global Parcellation of the Human Cerebral Cortex from Intrinsic Functional Connectivity MRI. *Cereb. Cortex* **28**, 3095–3114 (2018).

118. Markello, R. *et al.* neuromaps: structural and functional interpretation of brain maps. Zenodo https://doi.org/10.5281/ZENODO.5842498 (2024).

ARTICLE IN PRESS

ARTICLE IN PRESS

119. Markello, R. D. *et al.* neuromaps: structural and functional interpretation of brain maps. *Nat. Methods* **19**, 1472–1479 (2022).

120. Alexander-Bloch, A. F. *et al.* On testing for spatial correspondence between maps of human brain structure and function. *NeuroImage* **178**, 540–551 (2018).

121. Garyfallidis, E. *et al.* Dipy, a library for the analysis of diffusion MRI data. *Front. Neuroinformatics* **8**, (2014).

122. Hoopes, A., Mora, J. S., Dalca, A. V., Fischl, B. & Hoffmann, M. SynthStrip: skull-stripping for any brain image. *NeuroImage* **260**, 119474 (2022).

123. Billot, B. *et al.* SynthSeg: Segmentation of brain MRI scans of any contrast and resolution without retraining. *Med. Image Anal.* **86**, 102789 (2023).

124. Tournier, J.-D. *et al.* MRtrix3: A fast, flexible and open software framework for medical image processing and visualisation. *NeuroImage* **202**, 116137 (2019).

125. Veraart, J. *et al.* Denoising of diffusion MRI using random matrix theory. *NeuroImage* **142**, 394–406 (2016).

126. Veraart, J., Fieremans, E. & Novikov, D. S. Diffusion MRI noise mapping using random matrix theory. *Magn. Reson. Med.* **76**, 1582–1593 (2016).

127. Cordero-Grande, L., Christiaens, D., Hutter, J., Price, A. N. & Hajnal, J. V. Complex diffusion-weighted image estimation via matrix recovery under general noise models. *NeuroImage* **200**, 391–404 (2019).

128. Lee, H., Novikov, D. S. & Fieremans, E. Removal of partial Fourier-induced Gibbs (RPG) ringing artifacts in MRI. *Magn. Reson. Med.* **86**, 2733–2750 (2021).

129. Irfanoglu, M. O., Nayak, A., Taylor, P., Thai, A. & Pierpaoli, C. TORTOISEV4: ReImagining the NIH Diffusion MRI Processing Pipeline. *Imaging Neurosci.* https://doi.org/10.1162/IMAG.a.948 (2025) doi:10.1162/IMAG.a.948.

130. Andersson, J. L. R. & Sotiropoulos, S. N. An integrated approach to correction for off-resonance effects and subject movement in diffusion MR imaging. *NeuroImage* **125**, 1063–1078 (2016).

ARTICLE IN PRESS

ARTICLE IN PRESS

131. Andersson, J. L. R., Graham, M. S., Zsoldos, E. & Sotiropoulos, S. N. Incorporating outlier detection and replacement into a non-parametric framework for movement and distortion correction of diffusion MR images. *NeuroImage* **141**, 556–572 (2016).

132. Power, J. D. *et al.* Methods to detect, characterize, and remove motion artifact in resting state fMRI. *NeuroImage* **84**, 320–341 (2014).

133. Yeh, F.-C. *et al.* Differential tractography as a track-based biomarker for neuronal injury. *NeuroImage* **202**, 116131 (2019).

134. Richie-Halford, A. *et al.* An analysis-ready and quality controlled resource for pediatric brain white-matter research. *Sci. Data* **9**, 616 (2022).

135. Hagler, D. J. *et al.* Image processing and analysis methods for the Adolescent Brain Cognitive Development Study. *NeuroImage* **202**, 116091 (2019).

136. Basser, P. J., Mattiello, J. & LeBihan, D. MR diffusion tensor spectroscopy and imaging. *Biophys. J.* **66**, 259–267 (1994).

137. Jensen, J. H., Helpern, J. A., Ramani, A., Lu, H. & Kaczynski, K. Diffusional kurtosis imaging: The quantification of non-gaussian water diffusion by means of magnetic resonance imaging. *Magn. Reson. Med.* **53**, 1432–1440 (2005).

138. Jensen, J. H. & Helpern, J. A. MRI quantification of non-Gaussian water diffusion by kurtosis analysis. *NMR Biomed.* **23**, 698–710 (2010).

139. Henriques, R. N. *et al.* Diffusional Kurtosis Imaging in the Diffusion Imaging in Python Project. *Front. Hum. Neurosci.* **15**, 675433 (2021).

140. Zhang, H., Schneider, T., Wheeler-Kingshott, C. A. & Alexander, D. C. NODDI: Practical in vivo neurite orientation dispersion and density imaging of the human brain. *NeuroImage* **61**, 1000–1016 (2012).

141. Daducci, A. *et al.* Accelerated Microstructure Imaging via Convex Optimization (AMICO) from diffusion MRI data. *NeuroImage* **105**, 32–44 (2015).

ARTICLE IN PRESS

ARTICLE IN PRESS

142. Guerrero, J. M. *et al.* Optimizing the intrinsic parallel diffusivity in NODDI: An extensive empirical evaluation. *PLOS ONE* **14**, e0217118 (2019).

143. Parker, C. S. *et al.* Not all voxels are created equal: Reducing estimation bias in regional NODDI metrics using tissue-weighted means. *NeuroImage* **245**, 118749 (2021).

144. Özarslan, E. *et al.* Mean apparent propagator (MAP) MRI: A novel diffusion imaging method for mapping tissue microstructure. *NeuroImage* **78**, 16–32 (2013).

145. Yeh, Fang-Cheng, Wedeen, V. J. & Tseng, W.-Y. I. Generalized ${ q}$-Sampling Imaging. *IEEE Trans. Med. Imaging* **29**, 1626–1635 (2010).

146. Yeh, F.-C., Verstynen, T. D., Wang, Y., Fernández-Miranda, J. C. & Tseng, W.-Y. I. Deterministic Diffusion Fiber Tracking Improved by Quantitative Anisotropy. *PLoS ONE* **8**, e80713 (2013).

147. Yeh, F.-C. Shape analysis of the human association pathways. *NeuroImage* **223**, 117329 (2020).

148. Garyfallidis, E. *et al.* FURY: advanced scientific visualization. *J. Open Source Softw.* **6**, 3384 (2021).

149. Kruper, J. *et al.* Evaluating the Reliability of Human Brain White Matter Tractometry. *Aperture Neuro* **2021**, 25 (2021).

150. Wang, Z. *et al.* Empirical optimization of ASL data analysis using an ASL data processing toolbox: ASLtbx. *Magn. Reson. Imaging* **26**, 261–269 (2008).

151. Lanczos, C. Evaluation of Noisy Data. *J. Soc. Ind. Appl. Math. Ser. B Numer. Anal.* **1**, 76–85 (1964).

152. Buxton, R. B. *et al.* A general kinetic model for quantitative perfusion imaging with arterial spin labeling. *Magn. Reson. Med.* **40**, 383–396 (1998).

153. Dolui, S. *et al.* Structural Correlation-based Outlier Rejection (SCORE) algorithm for arterial spin labeling time series. *J. Magn. Reson. Imaging* **45**, 1786–1797 (2017).

ARTICLE IN PRESS

ARTICLE IN PRESS

154. Chappell, M. A., Groves, A. R., Whitcher, B. & Woolrich, M. W. Variational Bayesian Inference for a Nonlinear Forward Model. *IEEE Trans. Signal Process.* **57**, 223–236 (2009).

155. Chappell, M. A. *et al.* Partial volume correction of multiple inversion time arterial spin labeling MRI data. *Magn. Reson. Med.* **65**, 1173–1183 (2011).

156. Dolui, S. *et al.* Automated Quality Evaluation Index for Arterial Spin Labeling Derived Cerebral Blood Flow Maps. *J. Magn. Reson. Imaging* **60**, 2497–2508 (2024).

157. Desikan, R. S. *et al.* An automated labeling system for subdividing the human cerebral cortex on MRI scans into gyral based regions of interest. *NeuroImage* **31**, 968–980 (2006).

158. Glasser, M. F. *et al.* A multi-modal parcellation of human cerebral cortex. *Nature* **536**, 171–178 (2016).

159. Gordon, E. M. *et al.* Generation and Evaluation of a Cortical Area Parcellation from Resting-State Correlations. *Cereb. Cortex* **26**, 288–303 (2016).

160. Yeo, B. T. *et al.* The organization of the human cerebral cortex estimated by intrinsic functional connectivity. *J. Neurophysiol.* **106**, 1125–1165 (2011).

161. Garey, L. *Brodmann's Localisation in the Cerebral Cortex*. (Imperial College Press).

162. Pauli, W. M., Nili, A. N. & Tyszka, J. M. A high-resolution probabilistic in vivo atlas of human subcortical brain nuclei. *Sci. Data* **5**, 180063 (2018).

163. King, M., Hernandez-Castillo, C. R., Poldrack, R. A., Ivry, R. B. & Diedrichsen, J. Functional boundaries in the human cerebellum revealed by a multi-domain task battery. *Nat. Neurosci.* **22**, 1371–1378 (2019).

164. Najdenovska, E. *et al.* In-vivo probabilistic atlas of human thalamic nuclei based on diffusion-weighted magnetic resonance imaging. *Sci. Data* **5**, 180270 (2018).

165. Hermosillo, R. J. M. *et al.* A precision functional atlas of personalized network topography and probabilities. *Nat. Neurosci.* **27**, 1000–1013 (2024).

166. Tian, Y., Margulies, D. S., Breakspear, M. & Zalesky, A. Topographic organization of the human subcortex unveiled with functional connectivity gradients. *Nat. Neurosci.* **23**, 1421–1432 (2020).

ARTICLE IN PRESS

ARTICLE IN PRESS

167. Halchenko, Y. O. *et al.* HeuDiConv — flexible DICOM conversion into structureddirectory layouts. *J. Open Source Softw.* **9**, 5839 (2024).

168. Markiewicz, C. J. *et al.* The OpenNeuro resource for sharing of neuroscience data. *eLife* **10**, e71774 (2021).

169. Elyounssi, S. *et al.* Addressing artifactual bias in large, automated MRI analyses of brain development. *Nat. Neurosci.* **28**, 1787–1796 (2025).

170. Gilmore, A. D., Buser, N. J. & Hanson, J. L. Variations in structural MRI quality significantly impact commonly used measures of brain anatomy. *Brain Inform.* **8**, 7 (2021).

171. Power, J. D., Barnes, K. A., Snyder, A. Z., Schlaggar, B. L. & Petersen, S. E. Spurious but systematic correlations in functional connectivity MRI networks arise from subject motion. *NeuroImage* **59**, 2142–2154 (2012).

172. Reuter, M. *et al.* Head motion during MRI acquisition reduces gray matter volume and thickness estimates. *NeuroImage* **107**, 107–115 (2015).

173. Rosen, A. F. G. *et al.* Quantitative assessment of structural image quality. *NeuroImage* **169**, 407–418 (2018).

174. Satterthwaite, T. D. *et al.* Impact of in-scanner head motion on multiple measures of functional connectivity: Relevance for studies of neurodevelopment in youth. *NeuroImage* **60**, 623–632 (2012).

175. Van Dijk, K. R. A., Sabuncu, M. R. & Buckner, R. L. The influence of head motion on intrinsic functional connectivity MRI. *NeuroImage* **59**, 431–438 (2012).

176. Yan, C.-G. *et al.* A comprehensive assessment of regional variation in the impact of head micromovements on functional connectomics. *NeuroImage* **76**, 183–201 (2013).

177. Afacan, O. *et al.* Evaluation of motion and its effect on brain magnetic resonance image quality in children. *Pediatr. Radiol.* **46**, 1728–1735 (2016).

ARTICLE IN PRESS

ARTICLE IN PRESS

178. Fair, D. A. *et al.* Distinct neural signatures detected for ADHD subtypes after controlling for micro-movements in resting state functional connectivity MRI data. *Front. Syst. Neurosci.* **6**, (2013).

179. Thomson, P., Loosley, V., Friedel, E. & Silk, T. J. Changes in MRI head motion across development: typical development and ADHD. *Brain Imaging Behav.* **18**, 1144–1152 (2024).

180. Makowski, C., Lepage, M. & Evans, A. C. Head motion: the dirty little secret of neuroimaging in psychiatry. *J. Psychiatry Neurosci.* **44**, 62–68 (2019).

181. Pardoe, H. R., Kucharsky Hiess, R. & Kuzniecky, R. Motion and morphometry in clinical and nonclinical populations. *NeuroImage* **135**, 177–185 (2016).

182. Shi, T. C., Durham, K., Marsh, R. & Pagliaccio, D. Differences in Head Motion During Functional Magnetic Resonance Imaging Across Pediatric Neuropsychiatric Disorders. *Biol. Psychiatry Glob. Open Sci.* **5**, 100446 (2025).

183. Thomson, P., Loosley, V., Friedel, E. & Silk, T. J. Changes in MRI head motion across development: typical development and ADHD. *Brain Imaging Behav.* **18**, 1144–1152 (2024).

184. Kong, X. *et al.* Individual Differences in Impulsivity Predict Head Motion during Magnetic Resonance Imaging. *PLOS ONE* **9**, (2014).

185. Yao, N. *et al.* Inferring pathobiology from structural MRI in schizophrenia and bipolar disorder: Modeling head motion and neuroanatomical specificity. *Hum. Brain Mapp.* **38**, 3757–3770 (2017).

186. Klapwijk, E. T., Van De Kamp, F., Van Der Meulen, M., Peters, S. & Wierenga, L. M. Qoala-T: A supervised-learning tool for quality control of FreeSurfer segmented MRI data. *NeuroImage* **189**, 116–129 (2019).

187. Dolui, S. *et al.* Automated Quality Evaluation Index for Arterial Spin Labeling Derived Cerebral Blood Flow Maps. *J. Magn. Reson. Imaging* **60**, 2497–2508 (2024).

188. Van Essen, D. C. & Drury, H. A. Structural and Functional Analyses of Human Cerebral Cortex Using a Surface-Based Atlas. *J. Neurosci.* **17**, 7079–7102 (1997).

ARTICLE IN PRESS

ARTICLE IN PRESS

189. Huang, S. *et al.* Exploring the n-back task: insights, applications, and future directions. *Front. Hum. Neurosci.* **19**, 1721330 (2025).

190. Owen, A. M., McMillan, K. M., Laird, A. R. & Bullmore, E. N-back working memory paradigm: a meta-analysis of normative functional neuroimaging studies. *Hum. Brain Mapp.* **25**, 46–59 (2005).

191. Kochunov, P. *et al.* Relationship between white matter fractional anisotropy and other indices of cerebral health in normal aging: Tract-based spatial statistics study of aging. *NeuroImage* **35**, 478–487 (2007).

192. Tuch, D. S. Q-ball imaging. *Magn. Reson. Med.* **52**, 1358–1372 (2004).

193. Fang-Cheng Yeh, Wedeen, V. J. & Tseng, W.-Y. I. Generalized ${ q}$-Sampling Imaging. *IEEE Trans. Med. Imaging* **29**, 1626–1635 (2010).

194. Fieremans, E., Jensen, J. H. & Helpern, J. A. White matter characterization with diffusional kurtosis imaging. *NeuroImage* **58**, 177–188 (2011).

195. Hansen, B., Shemesh, N. & Jespersen, S. N. Fast imaging of mean, axial and radial diffusion kurtosis. *NeuroImage* **142**, 381–393 (2016).

196. Zhang, H., Schneider, T., Wheeler-Kingshott, C. A. & Alexander, D. C. NODDI: Practical in vivo neurite orientation dispersion and density imaging of the human brain. *NeuroImage* **61**, 1000–1016 (2012).

197. Burzynska, A. Z. *et al.* Correlates of axonal content in healthy adult span: Age, sex, myelin, and metabolic health. *Cereb. Circ. - Cogn. Behav.* **6**, 100203 (2024).

198. Sadikov, A., Choi, H. L., Xiao, J., Cai, L. T. & Mukherjee, P. Mapping the microstructure of human cerebral cortex in vivo with diffusion MRI. *Commun. Biol.* **8**, 1088 (2025).

199. Avram, A. V. *et al.* High-resolution cortical MAP-MRI reveals areal borders and laminar substructures observed with histological staining. *NeuroImage* **264**, 119653 (2022).

200. Warnert, E. A. H. *et al.* Implementation and validation of ASL perfusion measurements for population imaging. *Magn. Reson. Med.* **84**, 2048–2054 (2020).

ARTICLE IN PRESS

ARTICLE IN PRESS

201. Zhang, N., Gordon, M. L. & Goldberg, T. E. Cerebral blood flow measured by arterial spin labeling MRI at resting state in normal aging and Alzheimer's disease. *Neurosci. Biobehav. Rev.* **72**, 168–175 (2017).

202. Sevchik, B.L. *et al.* Penn LEAD: Penn Longitudinal Executive functioning in Adolescent Development - fMRIPrep Anatomical Derivatives. OpenNeuro. [Dataset]. https://doi.org/10.18112/openneuro.ds007089.v1.0.1 (2026).

203. Sevchik, B.L. *et al.* Penn LEAD: Penn Longitudinal Executive functioning in Adolescent Development - fMRIPrep Functional Derivatives. OpenNeuro. [Dataset]. https://doi.org/10.18112/openneuro.ds007088.v1.0.1 (2026).

204. Sevchik, B.L. *et al.* Penn LEAD: Penn Longitudinal Executive functioning in Adolescent Development - XCP-D Derivatives. OpenNeuro. [Dataset]. https://doi.org/10.18112/openneuro.ds007402.v1.0.2 (2026).

205. Sevchik, B.L. *et al.* PennLEAD: Penn Longitudinal Executive functioning in Adolescent Development - QSIPrep Derivatives. OpenNeuro. [Dataset]. https://doi.org/10.18112/openneuro.ds007090.v1.0.4 (2026).

206. Sevchik, B.L. *et al.* Penn LEAD: Penn Longitudinal Executive functioning in Adolescent Development - QSIRecon Derivatives. OpenNeuro. [Dataset]. https://doi.org/10.18112/openneuro.ds007091.v1.0.2 (2026).

207. Sevchik, B.L. *et al.* Penn LEAD: Penn Longitudinal Executive functioning in Adolescent Development - ASLPrep Derivatives. OpenNeuro. [Dataset]. https://doi.org/10.18112/openneuro.ds006744.v1.0.0 (2025).

ARTICLE IN PRESS